AD-A164 345 INVESTIGATION OF THE PLASMA PROPERTIES OF SURFACE 1/1
DISCHARGES(U) BEVERLY (R E) III AND ASSOCIATES COLUMBUS
OH R E BEVRRLY 30 SEP 85 REB85-804 ARO-22480.3-PH-S
UNCLASSIFIED DAAG29-84-C-0027 F/G 20/3 NL

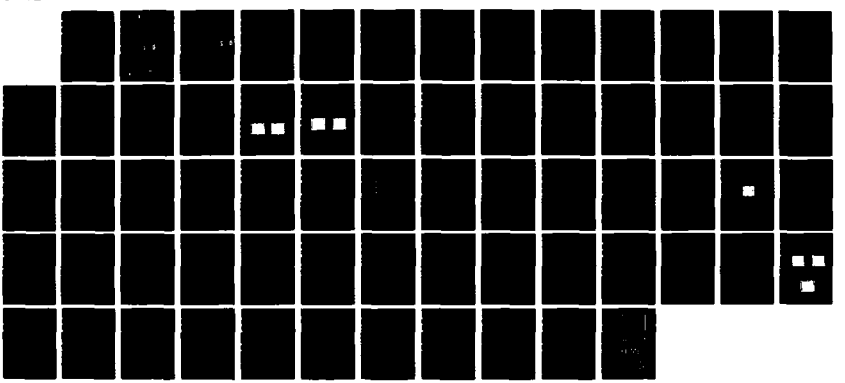

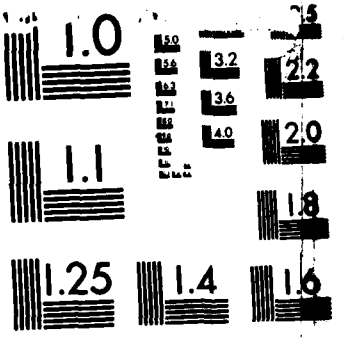

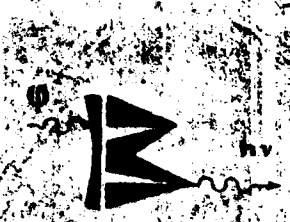

R. E. Beverly III and Associates
1891 Fishinger Road
Columbus, Ohio 43221
(614) 457-1242

Final Report

on

INVESTIGATION OF THE PLASMA PROPERTIES OF SURFACE DISCHARGES

September 30, 1985

(2)

Final Report

on

INVESTIGATION OF THE PLASMA PROPERTIES OF SURFACE DISCHARGES

September 30, 1985

Contract Number DAAH01-84-C-0027

by

R. E. Beverly III

R. E. BEVERLY III AND ASSOCIATES
1891 Fishinger Road
Columbus, Ohio 43221

Prepared for

U. S. ARMY RESEARCH OFFICE
P. O. Box 12211
Research Triangle Park, NC 27709

THE VIEWS, OPINIONS, AND/OR FINDINGS CONTAINED IN THIS REPORT ARE THOSE OF THE AUTHOR AND SHOULD NOT BE CONSTRUED AS AN OFFICIAL DEPARTMENT OF THE ARMY POSITION, POLICY, OR DECISION, UNLESS SO DESIGNATED BY OTHER DOCUMENTATION.

AD-A164345

UNCLASSIFIED

SECURITY CLASSIFICATION OF THIS PAGE (When Data Entered)

MASTER COPY - FOR REPRODUCTION PURPOSES

REPORT DOCUMENTATION PAGE		READ INSTRUCTIONS BEFORE COMPLETING FORM
1. REPORT NUMBER ARO 22480.3-PH-S	2. GOVT ACCESSION NO. N/A	3. RECIPIENT'S CATALOG NUMBER N/A
4. TITLE (and Subtitle) Investigation of the Plasma Properties of Surface Discharges		5. TYPE OF REPORT & PERIOD COVERED Final Report 1 Oct 1984-30 Sep 1985
		6. PERFORMING ORG. REPORT NUMBER REB85-004
7. AUTHOR(s) R. E. Beverly III		8. CONTRACT OR GRANT NUMBER(s) DAAG29-84-C-0027
9. PERFORMING ORGANIZATION NAME AND ADDRESS R. E. Beverly III and Associates 1891 Fishinger Road Columbus, OH 43221		10. PROGRAM ELEMENT, PROJECT, TASK AREA & WORK UNIT NUMBERS 22480-PH
11. CONTROLLING OFFICE NAME AND ADDRESS U. S. Army Research Office Post Office Box 12211 Research Triangle Park, NC 27709		12. REPORT DATE 30-Sep-85 13. NUMBER OF PAGES 60
14. MONITORING AGENCY NAME & ADDRESS(if different from Controlling Office)		15. SECURITY CLASS. (of this report) Unclassified 15a. DECLASSIFICATION/DOWNGRADING SCHEDULE

16. DISTRIBUTION STATEMENT (of this Report)

Approved for public release; distribution unlimited.

17. DISTRIBUTION STATEMENT (of the abstract entered in Block 20, if different from Report)

NA

18. SUPPLEMENTARY NOTES

The view, opinions, and/or findings contained in this report are those of the author(s) and should not be construed as an official Department of the Army position, policy, or decision, unless so designated by other documentation.

19. KEY WORDS (Continue on reverse side if necessary and identify by block number)

Surface discharges
Incoherent optical sources
Electrical properties
Breakdown time
Electrical recovery
Gasdynamic behavior
Shock waves
Optical detonation
Radiative properties
Spectroscopy

20. ABSTRACT (Continue on reverse side if necessary and identify by block number)

Large-area (60-220 cm^2), short-pulse (~1 μsec) planar discharges employing profiled electrodes have been produced across various polymer substrates. Parametric studies of the electrical circuit parameters and discharge dimensions demonstrate the importance of proper source-driver impedance matching to short-pulse operation. The degree of spatial homogeneity depends upon the peak discharge voltage, the initial rate of voltage rise, the specific capacitance of the substrate, the gas atmosphere and pressure, and the ablation mode of the substrate.

DD FORM 1 JAN 73 1473 EDITION OF 1 NOV 65 IS OBSOLETE

UNCLASSIFIED

SECURITY CLASSIFICATION OF THIS PAGE (When Data Entered)

Characteristic gap operating times for surface discharges in Ar at 1 atm pressure decrease from 200-300 nsec to <100 nsec as the charging voltage is raised from 10 kV to >20 kV for a 10-cm gap. The electrical recovery characteristics were measured using a secondary pulse of known amplitude applied to a tertiary electrode at a preset time delay following the main discharge. The electrical strength remains low for approximately 100 μsec and then recovers to almost complete pre-discharge hold-off capability within 300 μsec.

The velocities of shock waves induced by planar surface discharges in argon and xenon atmospheres were measured using miniature quartz piezoelectric gauges located perpendicular to the dielectric substrate. Measured wave velocities can be well correlated with the theory of a Chapman-Jouguet detonation despite the fact that the physical processes occurring here depart significantly from those in an optical detonation. Typical shock velocities are $D = 7(3) \times 10^4$ cm/sec for discharges in Ar(Xe) gas at 1 atm pressure and a discharge power density of $G = 5 \times 10^5$ W/cm^2.

Spectroscopic studies were performed to measure the equivalent brightness temperature, electron temperature, electron density, and optical thickness of smaller-area (24 cm^2) surface discharges across perovskite ceramic substrates. Detailed measurements were conducted with the spectrometer slit image perpendicular and parallel to the substrate surface, with the latter measurements being performed at incremental heights above the surface. The plasma is not opaque in the soft-uv and shows considerable structure due to line emission from neutral and singly-ionized species originating from the gas atmosphere and vaporized substrate material.

TABLE OF CONTENTS

LIST OF FIGURES

LIST OF TABLES

INTRODUCTION AND SUMMARY

Surface discharges offer numerous advantages as an ultraviolet (uv) source for lasers [1]. Some of these advantages include intense, short-pulsewidth emission which can be tailored for enhanced radiation in the spectral region of interest, scalability to large planar or cylindrical areas which are suitable for close-coupled excitation, life expectancies which can be extended to 10^6 flashes with proper engineering, simple and inexpensive designs which can withstand high-peak-power electrical loading without catastrophic failure, and capability for repetitively pulsed operation. Surface discharges are finding application as uv radiation sources to pump photodissociation excited media, to preionize carbon dioxide and excimer lasers, and to photoinitiate HF/DF chemical lasers [1,2]. Engineering considerations for incorporating surface discharges into pulsed lasers are given by the present author in Ref. [3].

Large-area (60-220 cm^2), short-pulse (~1 μsec) planar discharges employing profiled electrodes have been produced across various polymer substrates. All discharges were complete (i.e., completely bridged the anode-cathode gap) and operated in the moderate erosion regime ($E_d/A \sim 1$ J/cm^2). Parametric studies of the electrical circuit parameters and discharge dimensions demonstrate the importance of proper source-driver impedance matching to short-pulse operation. The degree of spatial homogeneity depends upon the peak discharge voltage, the initial rate of voltage rise, the specific capacitance of the substrate, the gas atmosphere and pressure, and the ablation mode of the substrate. Open-shutter photography, performed both perpendicular and parallel to the discharge plane, was used to develop criteria for obtaining uniform, coalesced discharges [2].

Characteristic "operating times" (time interval between application of high voltage to the gap and onset of appreciable current flow) for surface discharges in argon at 1 atm pressure decrease from 200-300 nsec to <100 nsec as the charging voltage is raised from 10 kV to >20 kV for a 10-cm gap. The electrical recovery characteristic were measured using a secondary pulse of known amplitude applied to a tertiary electrode at a preset time delay following the main discharge. These data, also for argon gas at 1 atm pressure, show that the electrical strength of the gap remains low for approximately 100 μsec and then recovers to almost complete pre-discharge hold-off capability within 300 μsec.

Surface discharges do not have an explosion limit analogous to flashlamps, although a shock wave is launched in a direction perpendicular to the dielectric substrate while the plasma itself remains tightly pressed against the substrate. For intracavity operation, the location of the surface discharge must be such that extraction of stored laser energy is effected prior

to the arrival of the shock wave at the boundary of the optically active region. The velocities of shock waves induced by planar surface discharges in argon and xenon atmospheres were measured using miniature piezoelectric gauges located perpendicular to and a few centimeters above the dielectric substrate. Measured wave velocities can be well correlated with the theory of a Chapman-Jouguet detonation despite the fact that the physical processes occurring here depart significantly from those in an optical detonation. Typical shock velocities are $D = 7(3) \times 10^4$ cm/sec for discharges in Ar(Xe) gas at 1 atm pressure and a discharge power density of $G = 5 \times 10^5$ W/cm^2.

Spectroscopic studies show that planar surface discharges radiate as Lambertian sources characterized by (visible) brightness temperatures T_b ~ 10,000-20,000 K. The plasma is not opaque in the soft uv and shows considerable structure due to line emission from neutral and singly-ionized species originating from the gas atmosphere and vaporized substrate material. Radiative output for the rare gases is proportional to the atomic weight to the two-thirds power. The presence of line transitions from vaporized and excited substrate species can greatly enhance the radiative output, especially in the uv and vuv spectral regions. Using smaller-area (24 cm^2) discharges across perovskite ceramic substrates, measurements with the spectrometer slit image perpendicular and parallel to the substrate surface show that T_b(parallel) ~ $1.5T_b$(perpendicular) and the optical thickness $\tau \sim 0.2$. Electron densities inferred from Stark broadening of the H-alpha line yielded values of $n_e = 10^{16}$-10^{17} cm^{-3}. The electron temperature was measured using Boltzmann's graphical method and gave a value of $T_e \sim 2$ eV.

Attempts to observe a population inversion on the Sr II ion transitions at 416.18 and 430.55 nm via plasma recombination in a surface discharge proved unsuccessful. The discharge conditions here were far from ideal, and use of a different substrate material, a shorter current pulsewidth, a larger specific input energy, and a higher He diluent pressure should result in more nearly optimum conditions.

EXPERIMENTAL ARRANGEMENT

Source Geometry

The geometry of the planar surface discharge source and an equivalent circuit schematic are shown in Fig. 1. The discharge width and gap are given by w and d, respectively, and the source area is A. Experiments were performed with Chang [4] profile and parallel electrodes of various widths. The Chang profile electrodes were electric-discharge machined with parameters $k = 0.0403$, $\upsilon = 1.5110$, $x_m = 3.9370$", and $y_0 = 3.0000$". The electrode material is brass or stainless steel, depending upon the gas mixture under investigation.

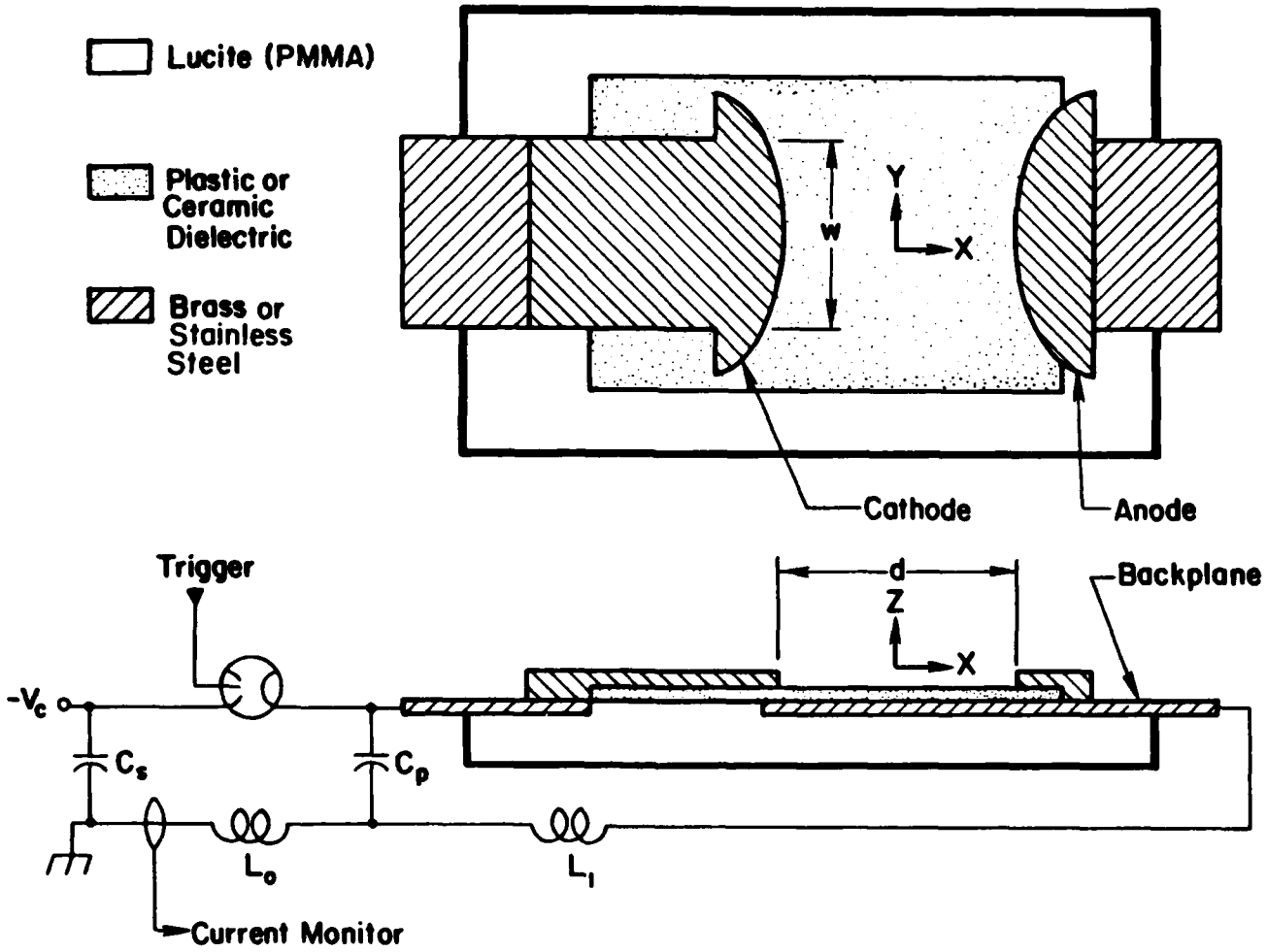

Fig. 1. Surface-discharge geometry and equivalent circuit.

A potential sufficient for breakdown of the interelectrode gap is applied producing plasma adjacent to the surface of the dielectric substrate. The presence of a conductive backplane permits current to flow prior to gap closure. Thus, the leader experiences a displacement current because of the presence of distributed capacitance in the gap. The specific capacitance of the dielectric substrate is

$$C_{sp}\ (pF/cm^2) = 0.88\ \varepsilon/\Delta, \qquad (1)$$

where ε is the dielectric constant and Δ is the substrate thickness (mm). The surface-discharge geometry shown permits breakdown of gaps at much lower potentials than for equivalent free sparks. Tables I and II list properties of the plastic and ceramic dielectric substrates used in these experiments. The dissipation factor $D = \tan\delta$, where δ is the loss angle, is the ratio of the imaginary and real components of the dielectric permittivity.

The large-area surface-discharge source employing plastic dielectric substrates is contained in a Plexiglas® housing with strip-line electrical feeds. The small-area source employing ceramic dielectric substrates used specifically for the recombination laser studies is mounted inside a stainless-steel chamber and fed using RG-217/U coaxial cable. The radiation is viewed either through the Plexiglas® housing or through quartz or lithium fluoride windows. Prior to discharge, the enclosure is evacuated to a pressure of approximately 700 μ for the Plexiglas® housing and 20 μ for the stainless chamber using a mechanical vacuum pump and then filled with the desired gas atmosphere. Research purity gases (>99.95%) were used unless otherwise specified.

TABLE I. Plastic dielectric substrate properties.

Material	Density, g/cm^3	Dielectric constant, ε	Dissipation factor, $\tan\delta$	Dielectric strength, V/mil
Polyethylene	0.966	2.30-2.35	0.00008-0.0001	450-500
Polyethylene terephthalate		3.37	0.021	560
Polytetra-fluoroethylene	2.10	2.10	0.00006	480
Fiberglass		3.5-6.4	0.008-0.22	345-420
Cellulose acetate		3.2-7.0	0.01-0.10	250-600
Polymethyl-methacrylate		2.63-2.76	0.039	490

Dielectric constant and dissipation factor measured at 1 MHz.

TABLE II. Ceramic dielectric substrate properties.

Material	Crystalline form	Theoretical (actual) density, g/cm^3	Melting point, C	Dielectric constant, ε
Strontium titanate ($SrTiO_3$)	Cubic	5.11 (75%)	2040	300
Strontium zirconate ($SrZrO_3$)	Orthorhombic	5.48 (79%)	>2700	

Dielectric constant measured at 1 MHz.

Electrical Driver

The main energy storage capacitor C_s is charged to a voltage V_c with a stored energy of

$$E_s = 0.5\ C_s V_c^2, \tag{2}$$

and is discharged into the load by two parallel N_2-pressurized spark gaps. The deposited energy is

$$E_d = \eta_d E_s, \tag{3}$$

where η_d is the discharge electrical efficiency. Peaking capacitors C_p are used to increase the current and optical rise time at the load. The total circuit inductance is

$$L = L_0 + L_1. \tag{4}$$

Current waveforms are measured using an Ion Physics Company Model CM-1-S current monitor, while voltage waveforms are measured using a custom-built coaxial divider.

Time-Integrated Spectroscopy

The optical diagnostics system and overall experimental arrangement are shown by the plan view in Fig. 2. A Tracor-Northern Diode Array Rapid Scan Spectrometer (DARSS) is used to obtain time-integrated quantitative spectra. The intensified diode array detector contains 1024 elements (25 μm x 0.432 mm each) which can span 40 nm or 300 nm in a single exposure depending upon which grating is employed in the spectrometer. The Ebert spectrometer has a 0.5-m focal length, an f/8.6 aperture, and a reciprocal linear dispersion of 1.6 nm/mm (1180 grooves/mm, 190-nm blaze grating) or 12.8 nm/mm (147.5 grooves/mm, 300-nm blaze grating).

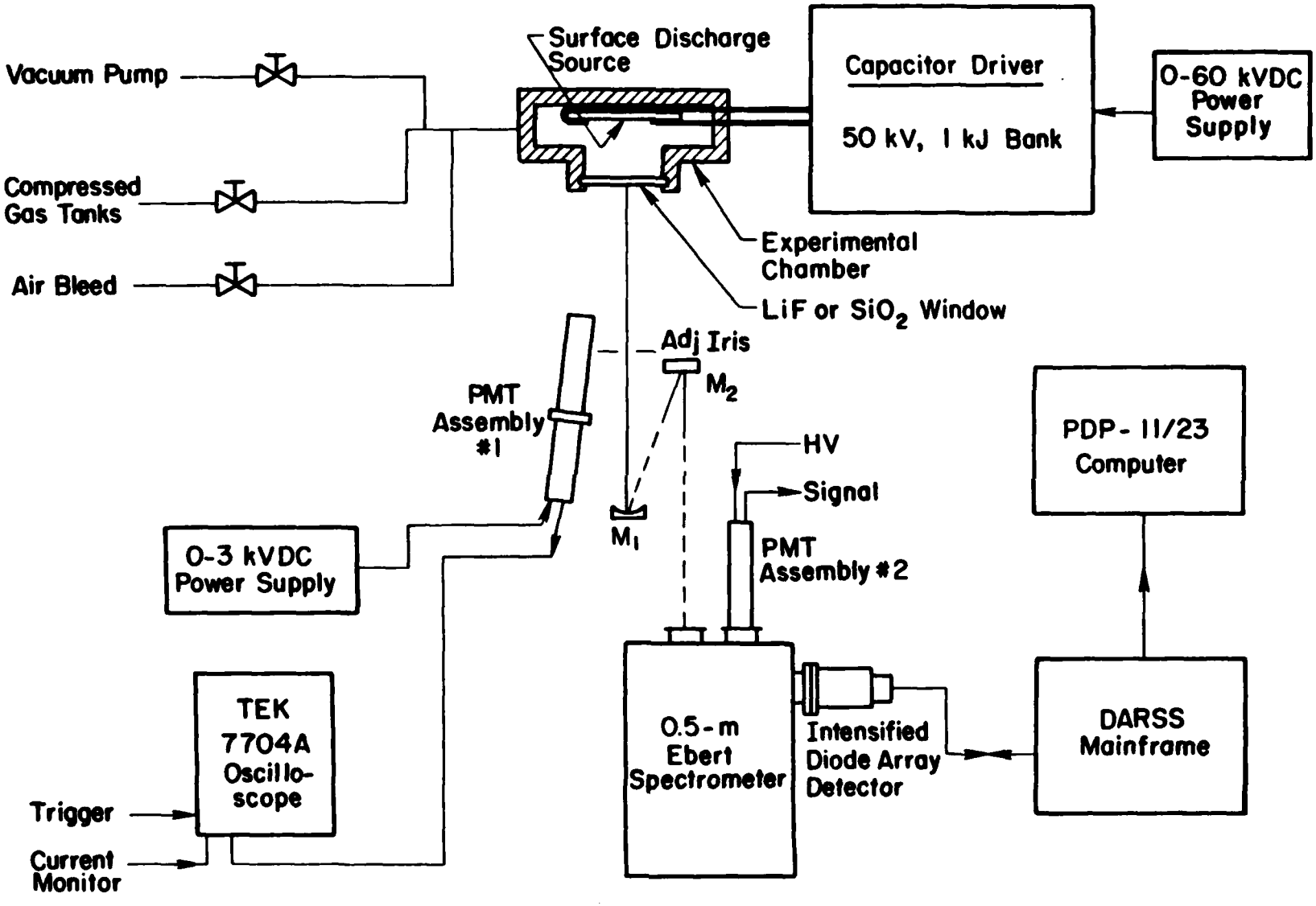

Fig. 2. Optical diagnostics system and experimental arrangement.

The optical transfer system, consisting of spherical mirror M_1, flat mirror M_2, and an adjustable iris, enables the spectrometer to sample light subtending a small solid angle from a small area of the discharge plasma. Positioning of the mirrors is such that the discharge area sampled is equal to the entrance slit area (1:1 optical transfer system). The adjustable entrance slit was set to a width of 50 μm and a height of 6 mm thus completely filling the diode elements. Both mirrors are uv-enhanced aluminum overcoated with a MgF_2 dielectric. Alignment of the optical transfer system is accomplished using a HeNe laser (not shown) which is projected into the spectrometer exit slit. The entire optical train is therefore traced out and a method is established for locating the slit image precisely on the radiating source.

Wavelength calibration of the DARSS system is performed using a low pressure Hg-Ar arc lamp. Computerized wavelength calibration was performed by a polynomial least-squares fit to the Hg line positions giving wavelength uncertainties of 0.03 nm and 0.2 nm for the high- and low-dispersion gratings, respectively. The corresponding instrumental widths are approximately 0.04 nm and 0.3 nm. The optical transfer system, spectrometer, and DARSS were calibrated as a system using an NBS-traceable standard of spectral radiance (Optronics Laboratories model 550C lamp). The approximate uncertainty in the lamp calibration ranges from +/-3% in the visible to a maximum of +/-5% at 250 nm.

Data from the DARSS mainframe were downloaded to a PDP-11/23 computer for archival storage, analysis, and plotting. Wavelength and spectral radiance calibration data were used along with specially developed software to give plots of the integrated spectral radiance as a function of wavelength and to integrate these data to yield radiant excitance values for various pumpbands. Calibration data thus generated are shown in Fig. 3 for several different intensifier gain settings.

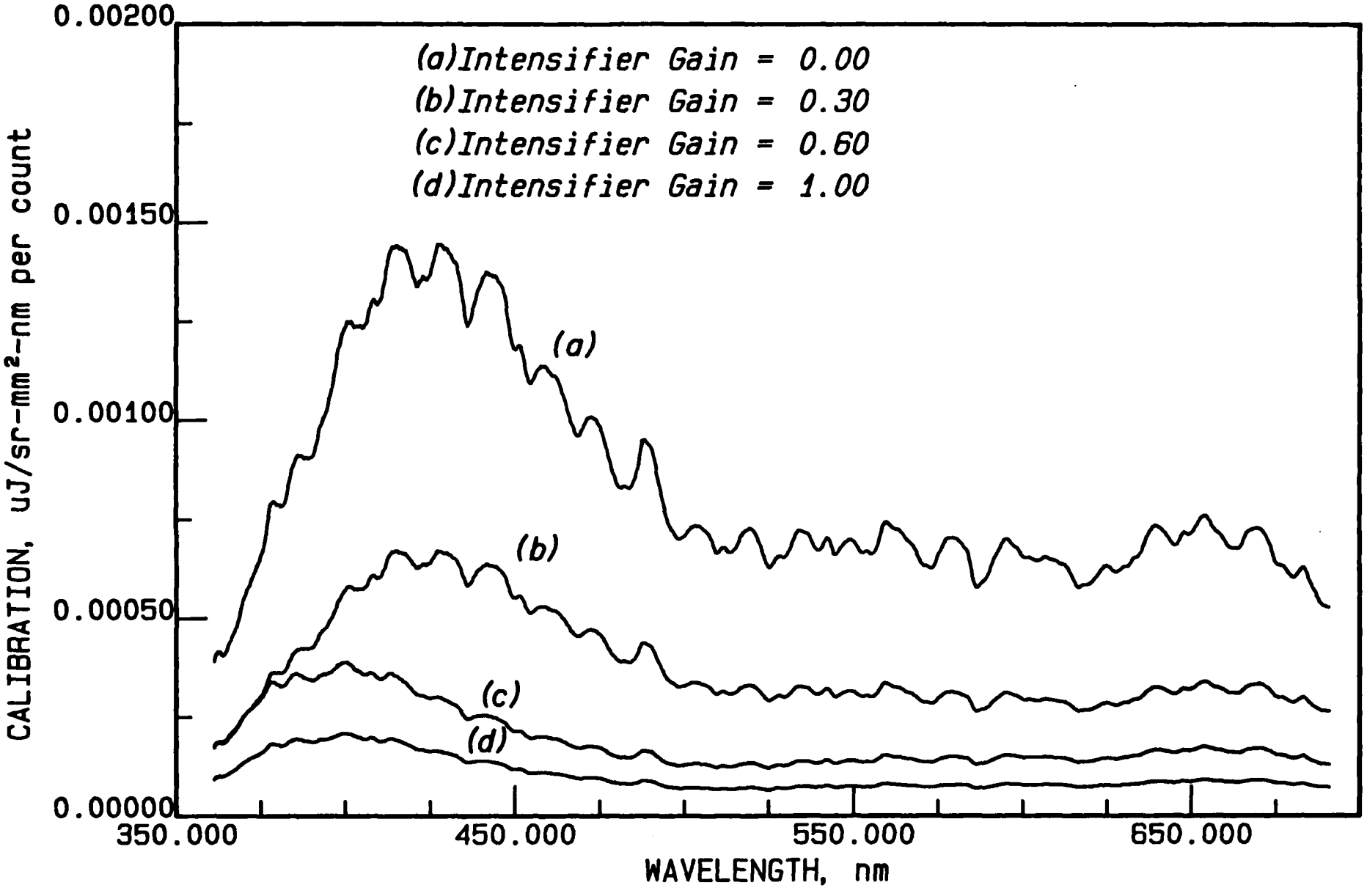

Fig. 3. DARSS integrated spectral radiance calibration curves.

Time-Dependent Spectroscopy

Two photomultiplier (Hamamatsu R-1509) assemblies were used to measure temporal dependencies. Assembly #1 is used in conjunction with various bandpass filter/pinhole aperture arrangements to measure optical pulse shapes, while assembly #2 is used to follow the temporal evolution of line species in the discharge. Assembly #2 is located at the exit slit of the Ebert spectrometer which provides alternate outputs for the PMT or DARSS via an internal pivoting mirror. Both PMT assemblies were calibrated using chopped radiation from the spectral radiance standard. Signals from the PMTs, current, and voltage monitors were recorded using a TEK 7704A oscilloscope with C-51 camera.

Representative broadband (λ = 267 nm, $\Delta\lambda$ = 30 nm) optical pulseshape traces are shown in Fig. 4 for discharges in 1 atm Ar and Xe. Note that the PMT gain in Fig. 4(a) is equal to that in Fig. 4(b); hence the peak optical intensity produced by discharges in Xe gas is 4.1 times that for operation in Ar under identical conditions. The optical pulsewidths are 1.8 and 1.3 μsec (FWHM) for discharges in Ar and Xe gas, respectively. The optical decay time is longer than the rise time, especially for discharges in Ar. This is due to a lower plasma resistance for Ar discharges resulting in a lower electrical damping coefficient.

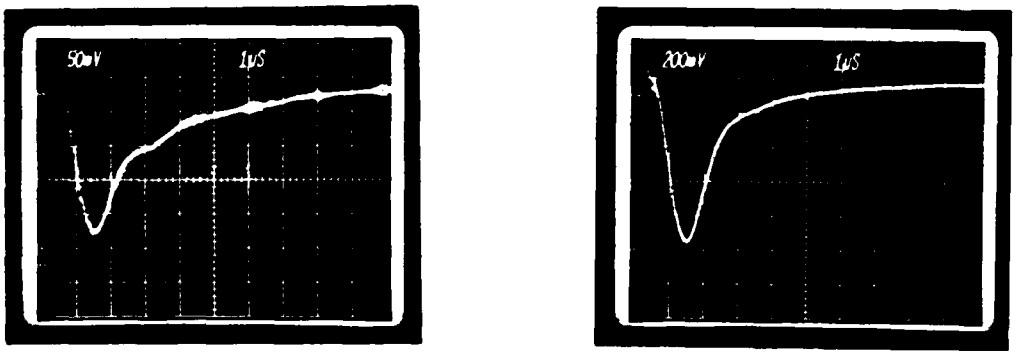

a b

Fig. 4. Representative optical pulseshapes for a 10 x 10 cm^2 planar discharge across cellulose acetate (C_{sp} = 4.2 pF/cm^2) in (a) 1 atm Ar and (b) 1 atm Xe. Electrical parameters are C_s = 868 nF, C_p = 6.6 nF, L = 284 nH, and V_c = 15 kV.

DISCHARGE ELECTRICAL PROPERTIES

Surface discharges are inherently low-impedance (< 1Ω) loads. The condition for critical damping of the current waveform,

$$Z_d = 0.5\ Z_s, \tag{5}$$

where Z_d and Z_s are the driver and source impedances, respectively, is also the condition required to maximize the power into the source load [1]. For a purely reactive driver,

$$Z_d = (L/C_s)^{1/2}, \tag{6}$$

requiring low-inductance circuitry for short optical pulsewidths. Current waveforms for all the experiments reported here are oscillatory or near-critically damped as shown by the typical traces in Fig. 5 (0.31-MHz ring frequency). The peak radiation intensity in the visible and soft-uv occurs temporally coincident with the peak current.

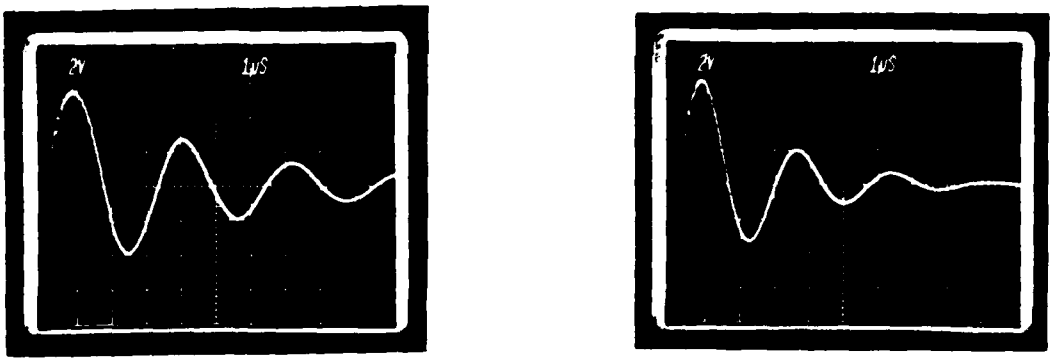

a b

Fig. 5. Representative current waveforms for a 10 x 10 cm^2 planar discharge across cellulose acetate (C_{sp} = 4.2 pF/cm^2) in (a) 1 atm Ar and (b) 1 atm Xe. Electrical parameters are C_s = 868 nF, C_p = 6.6 nF, L = 284 nH, and V_c = 22.5 kV. The scale is 1 V = 5 kA.

The total circuit inductance and resistance can be determined using the following relations from elementary circuit analysis:

$$L = [(t_2-t_1)/(2n)]^2(1 - \zeta^2)/C_s \tag{7}$$

and

$$R = 2L/(t_2-t_1)\ \ln(i_1/i_2), \tag{8}$$

where ζ is the damping ratio, i.e. the actual total resistance divided by the resistance for critical damping,

$$\zeta = R/[2(L/C_s)^{1/2}]. \tag{9}$$

Here, (i_1,t_1) and (i_2,t_2) are the measured current and time for the first and second peaks in the waveform. For the case of $\zeta << 1$, then Eqs. (7) and (8) are solved directly; otherwise, an iterative method is used. The external circuit resistance, R_{ext}, and total circuit inductance L were determined using this method while shorting the surface-discharge source with brass shim stock. The value of L_0 was determined similarly by shorting the capacitor bank at the end of the transmission line. The value of $L_1 = L - L_0$ could then be calculated. Measured circuit parameters for the two experimental configurations are summarized in Table III.

TABLE III. Measured circuit parameters.

Experiment(s)	Transmission Line	L_0, nH	L_1, nH	L, nH	R_{ext}, mΩ
Breakdown time Electrical recovery Shock velocities	Strip line	229±16	55±10	284±15	56±4
Non-Boltzmann behavior	RG-217/U	--	--	630±15	120±6

If R is the total circuit resistance as determined using Eq. (8) under normal discharge operation, the surface-discharge load resistance can be approximated by the relation

$$R_{sd} = R - R_{ext} \tag{10}$$

and the discharge efficiency can be estimated using the relation

$$\eta_d = E_d/E_s = R_{sd}/R. \tag{11}$$

Analysis of current waveforms as described above shows that the source resistance, as plotted in Fig. 6, increases with the gap d, for $d >> d_{sh}$, where d_{sh} is the characteristic electrode sheath dimension. Thus, for a given V_c, d can be increased to a value for which the critical damping requirement is satisfied provided, of course, that the value of V_c is sufficient for gap breakdown. The source resistance also decreases with charging voltage. Because the resistance determined in this manner is a weighted average over one current cycle, we can conclude that this decrease is associated with plasma expansion during this period and a concomitant increase in the plasma cross-sectional area.

The source resistance is not directly proportional, however, to the reciprocal of the discharge width, 1/w. As shown in Fig. 7, the plasma can expand laterally to an area greater than the nominal source dimensions (w x d) for 10-cm-wide electrodes due to the presence of the 20-cm-wide conductive backplane in the large-area source. For $d < w$ [Fig. 7(a)], the plasma shows little lateral spread beyond the nominal electrode width. For $d = w$ [Fig. 7(b)], the plasma is bowed outward; for $d > w$ [Fig. 7(c)], the lateral extent of the plasma greatly exceeds the discharge width and the plasma tends to wrap around the electrode extensions. For this reason, the functional dependence of the plasma resistance for the 10-cm-wide electrodes exhibits complex behavior and is not simply double that for the 20-cm electrodes. The source resistance is larger with Xe gas than for Ar. Also, the source resistance decreases with increasing C_s. When the energy storage capacitance is comparable to the total distributed capacitance of the surface-discharge source ($C_s \sim AC_{sp}$), then most of the stored charge goes into the displacement current driving the spark leaders and the inferred resistance is high.

Because of the low impedance of the load, the discharge electrical efficiency depends sensitively on external losses such as the characteristic loss resistance of the capacitor(s) and the transmission line resistance. Every effort should be made to minimize these losses if the electrical-to-optical conversion efficiency is important. Comprehensive parametric studies of R_{sd} as a function of w, d, C_s, and the gas type are given by the present author in Refs. [5,6].

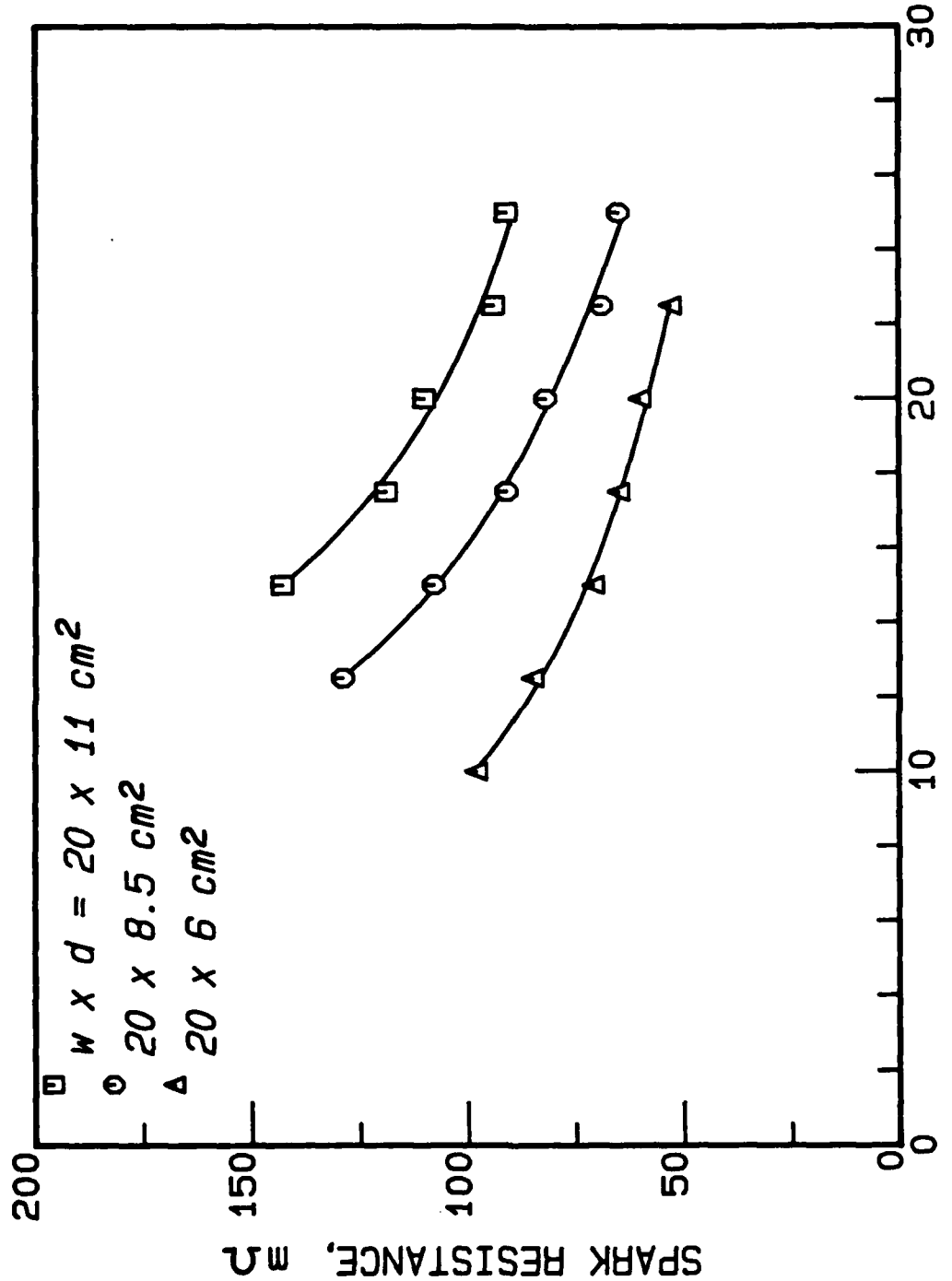

Fig. 6. R_{sd} as a function of V_c (w = 20 cm, 1 atm Ar).

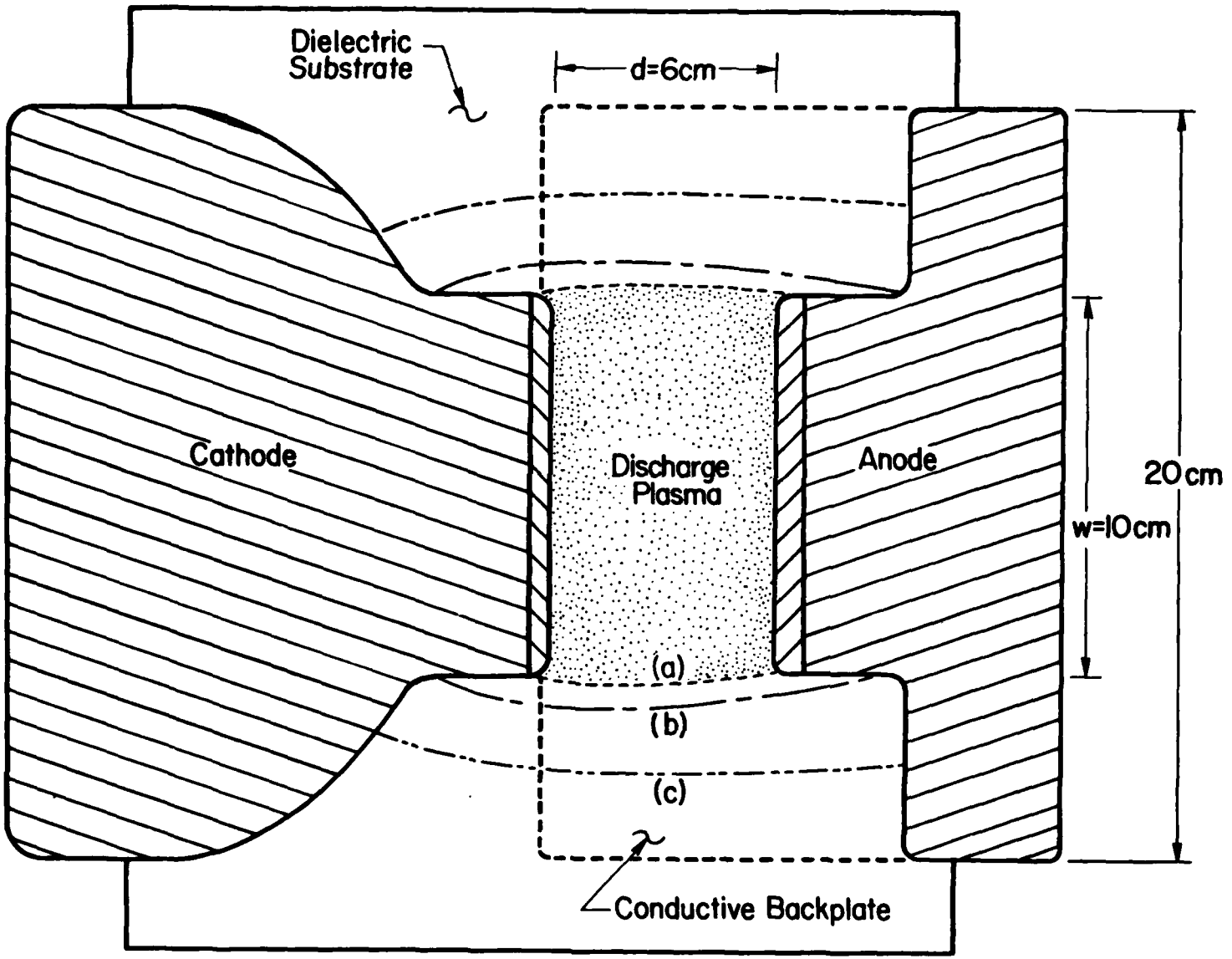

Fig. 7. Plasma expansion characteristics for 10-cm-wide discharges.

The peak current, I_p, shows a weak dependence on the gas type, gas pressure, and dielectric material and thickness through influence of these parameters on ζ as shown in Figs. 8 and 9. The functional dependence of the peak current is in accordance with the relation derived from elementary circuit analysis,

$$I_p = V_c (C_s/L)^{1/2} \exp(-\pi\zeta/2), \qquad \zeta^2 << 1. \tag{12}$$

The time at which the maximum current is observed increases with increasing C_s and decreases with decreasing L, also in accordance with elementary circuit analysis:

$$t(I_p) = 0.5\,\pi(LC_s)^{1/2}, \qquad \zeta^2 << 1. \tag{13}$$

Note that the initial rate of current rise is independent of the type of discharge ($\zeta < 1$, underdamped; $\zeta = 1$, critically damped; $\zeta > 1$, overdamped):

$$dI/dt|_0 = V_c/L. \tag{14}$$

The value of V_c/L is sometimes referred to as the "hardness" of the discharge. Note that in Figs. 6 and 9, open symbols correspond to polyethylene terephthalate dielectric (C_{sp} = 11.7 pF/cm^2) while solid symbols denote cellulose acetate dielectric (C_{sp} = 4.2 pF/cm^2).

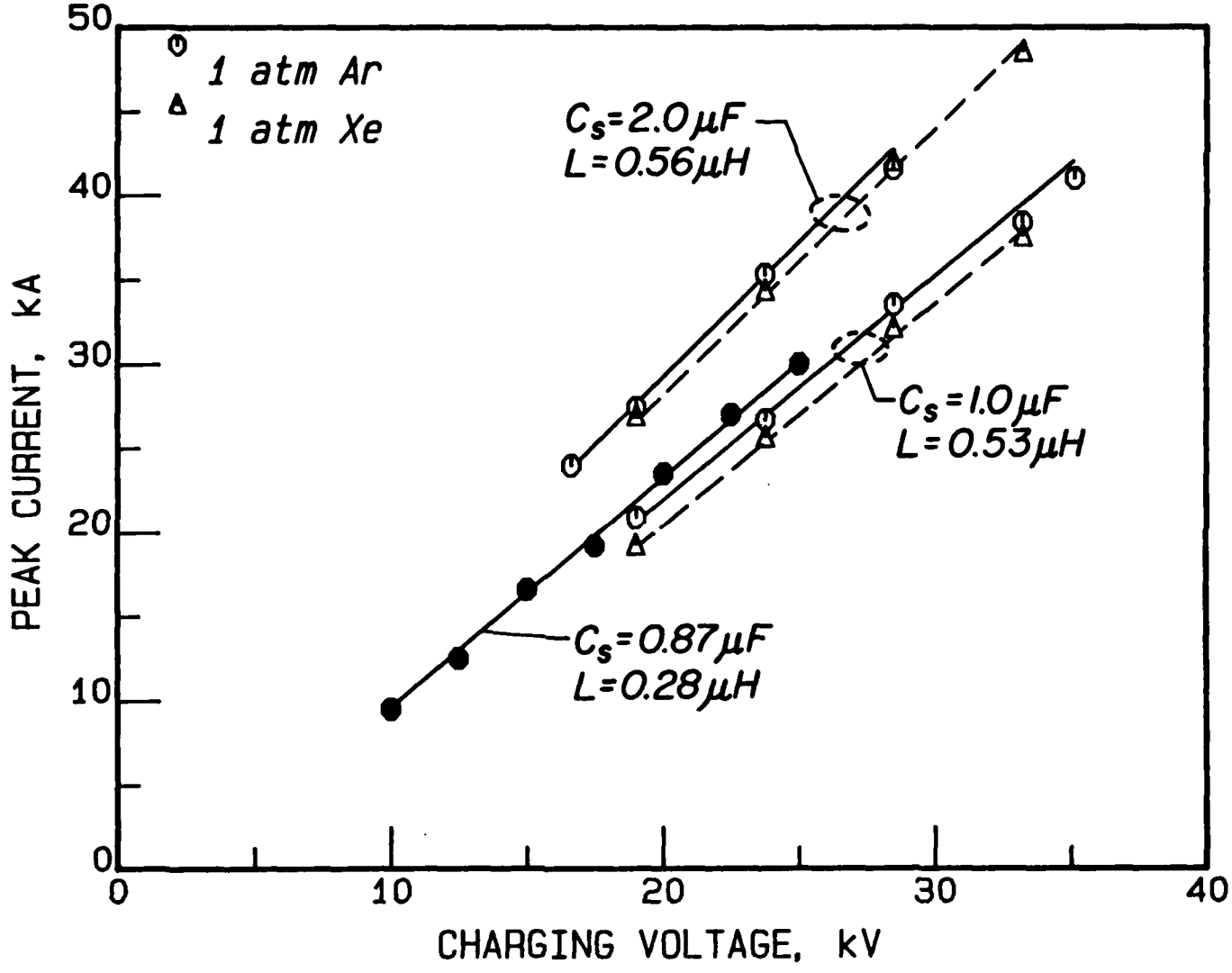

Fig. 8. I_p as a function of V_c, C_s, L, and gas type. Data for the 1- and 2-uF cases are for 4 x 4 cm^2 discharges across chromium oxide and are taken from the work of Beverly et al. [5]. Data for the 868-nF case is for 10 x 11 cm^2 discharges across cellulose acetate.

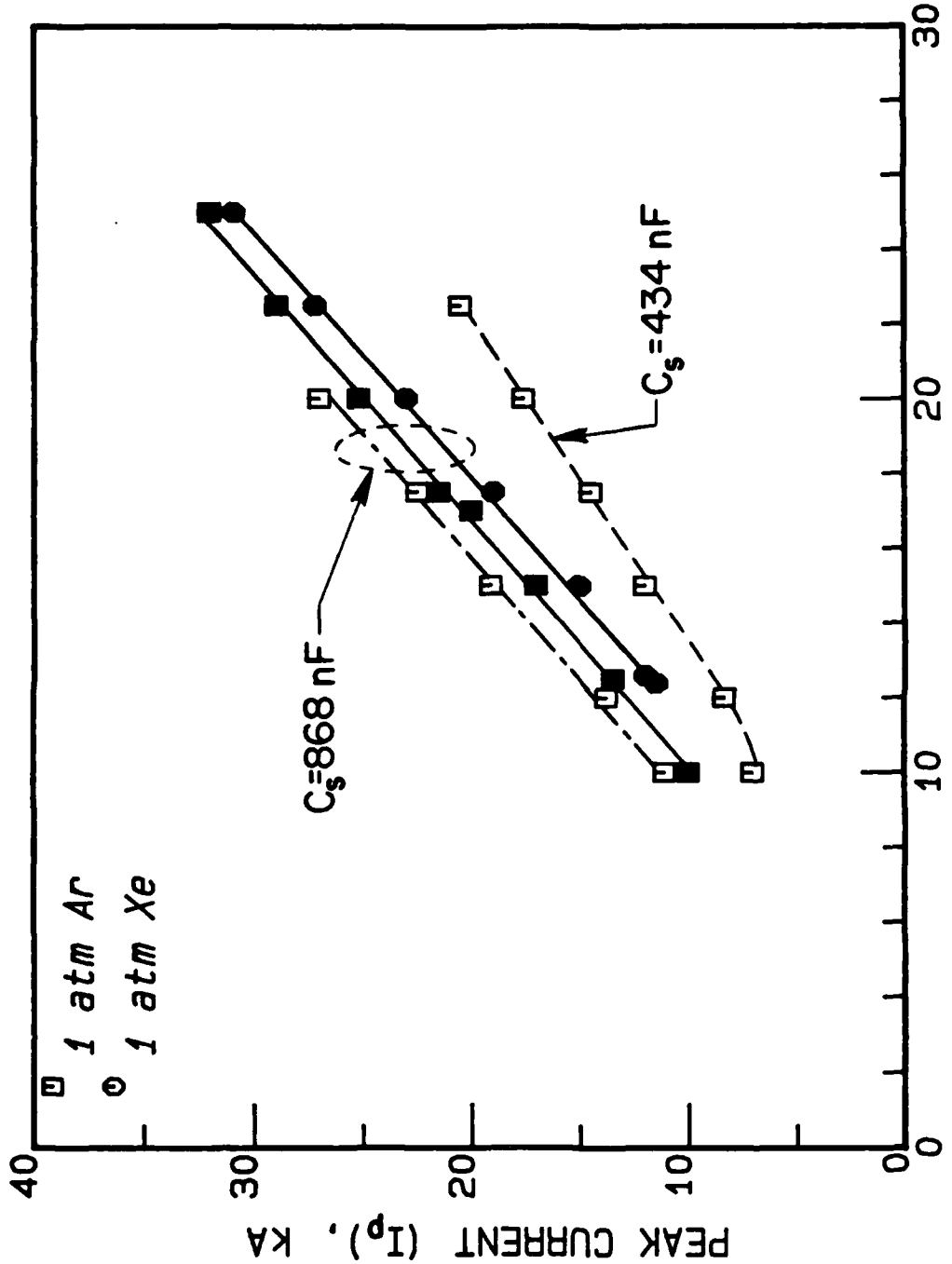

Fig. 9. I_p as a function of V_c, C_s, gas type, and dielectric substrate.

The presence of peaking capacitors C_p induces a voltage on the load which is larger than the charging voltage V_c. The peak voltage on the peaking capacitors, V_p, occurs approximately at time

$$t(V_p) = \pi(LC)^{1/2}, \qquad \zeta^2 << 1 \tag{15}$$

and can be derived as follows:

$$V_p/V_c = \beta(2 - \pi\zeta)/(\beta + 1), \qquad \zeta^2 << 1, \tag{16}$$

where β is the ratio of capacitances

$$\beta = C_s/C_p, \tag{17}$$

C is the total series capacitance

$$1/C = 1/C_s + 1/C_p, \tag{18}$$

and it is assumed that $R_{sd} = \infty$ until $t = t(V_p)$. The applicability the latter assumption is questionable for this type of discharge since the gap breakdown phase is accompanied by a displacement current as discussed previously, so Eq. (16) should be used with caution. Addition of peaking capacitors to practical discharge circuits produces an increase in I_p at the load while causing a decrease in $dU/dt|_0$.

ELECTRICAL BREAKDOWN AND RECOVERY CHARACTERISTICS

Measurement of Characteristic Breakdown Times

The temporal characteristics of a surface discharge can be defined by examining the current (I) and voltage (U) waveforms, registered simultaneously, for the discharge gap. We adopt the same nomenclature as defined by Belyaev et al. [7]. The operating time, t_{op}, is the elapsed time between application of the voltage pulse and appearance of appreciable current flow (defined here as $0.1I_p$). As shown by the typical oscilloscope traces in Fig. 10, the operating time is composed of the delay time, t_d, and the switching time, t_s:

$$t_{op} = t_d + t_s. \tag{19}$$

The delay time t_d is the time required for formation of plasma channels which place the gap in a conductive state. The delay time includes the time interval during which the (absolute) voltage on the cathode increases from zero to a level at which leaders form and travel toward the anode. The (absolute) voltage peaks when these leaders reach the anode. The increase in gap conductivity is accompanied by a collapse in voltage followed by an increase in current. The time interval from peak voltage (U_p) until the appearance of appreciable current ($0.1I_p$) is defined as the switching time t_s.

Experiments were performed in which these characteristic times were parameterized as a function of V_c for planar surface discharges in Ar gas at 1 atm pressure. Discharges were struck across polyethylene terephthalate substrates (Δ = 0.38 mm, C_{sp} = 7.8 pF/cm^2) with an active area of A = w x d = 10 x 10 cm^2. As shown in Fig. 11, the delay time t_d is observed to decrease slowly with increasing V_c; t_d is insensitive to the value of C_s, within experimental error, but depends more directly on the value of initial voltage rise $dU/dt|_0$ [7]. For these experimental conditions, $dU/dt|_0$ = (1-3) x 10^{11} V/sec and these data are comparable to those of Belyaev et al. [7] for discharges in air triggered by applying a high-voltage pulse of opposite polarity to a control electrode placed between the cathode and anode. The operating and switching times, as shown in Figs. 12 and 13, are substantially shorter for these measurements in Ar than for Belyaev's measurements in air. This is presumably because the breakdown leader bridges the gap in a single stroke for overvoltaged discharges in Ar gas, while repeatedly extinguishing and reforming for air discharges, thereby bridging the gap in a discontinuous fashion [8] and thus requiring more time. t_{op} and t_s are both larger for the larger value of C_s, because $dU/dt|_0$ lies in the lower end of the range quoted above. As V_c increases, the respective curves for t_s and t_{op} with the two values of C_s merge and the effects of different storage capacitances cannot be distinguished. Note that the curves for t_s shown in Fig. 13 were obtained by subtracting the best-fit values of t_d from the corresponding best-fit values of t_{op} and, hence, no data points are shown.

It is difficult to compare these results with theory without further information on the characteristics of the formative leaders. For example, Johnson et al. [9] developed semiempirical formulas for the formative time lag in multichannel rail-gap switches. The formative time lag, t_f, is defined as the time for the voltage across the switch to collapse from 90% to 10% of its static value and is roughly equivalent to t_s. t_f is comprised of inductive and resistive components which are comparable in magnitude for a rail-gap switch. Calculation of the inductive component requires estimation of the number and inductance of individual leader channels and the formula for the resistive component is probably not applicable to surface discharges.

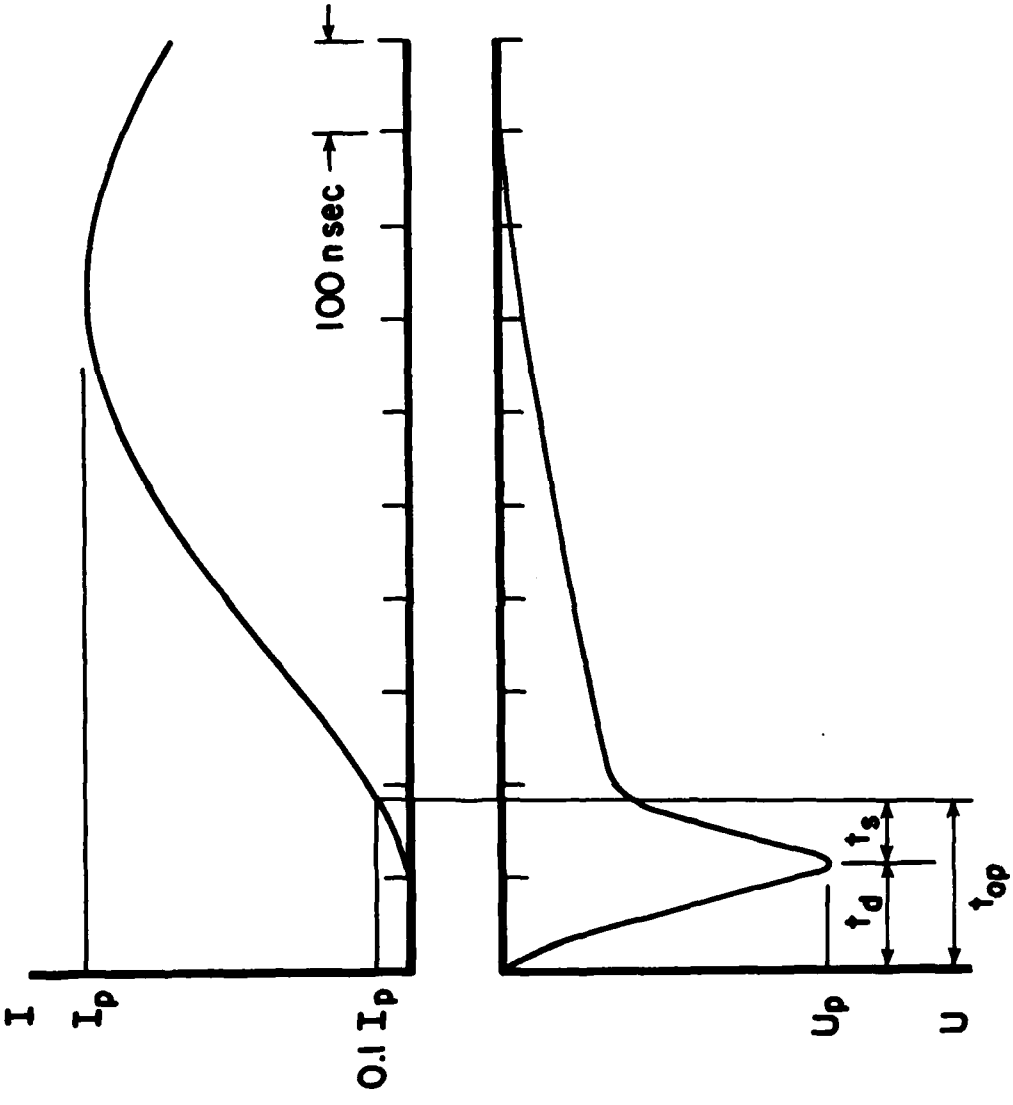

Fig. 10. Typical oscilloscope traces of surface-discharge current and voltage showing times relevant for breakdown.

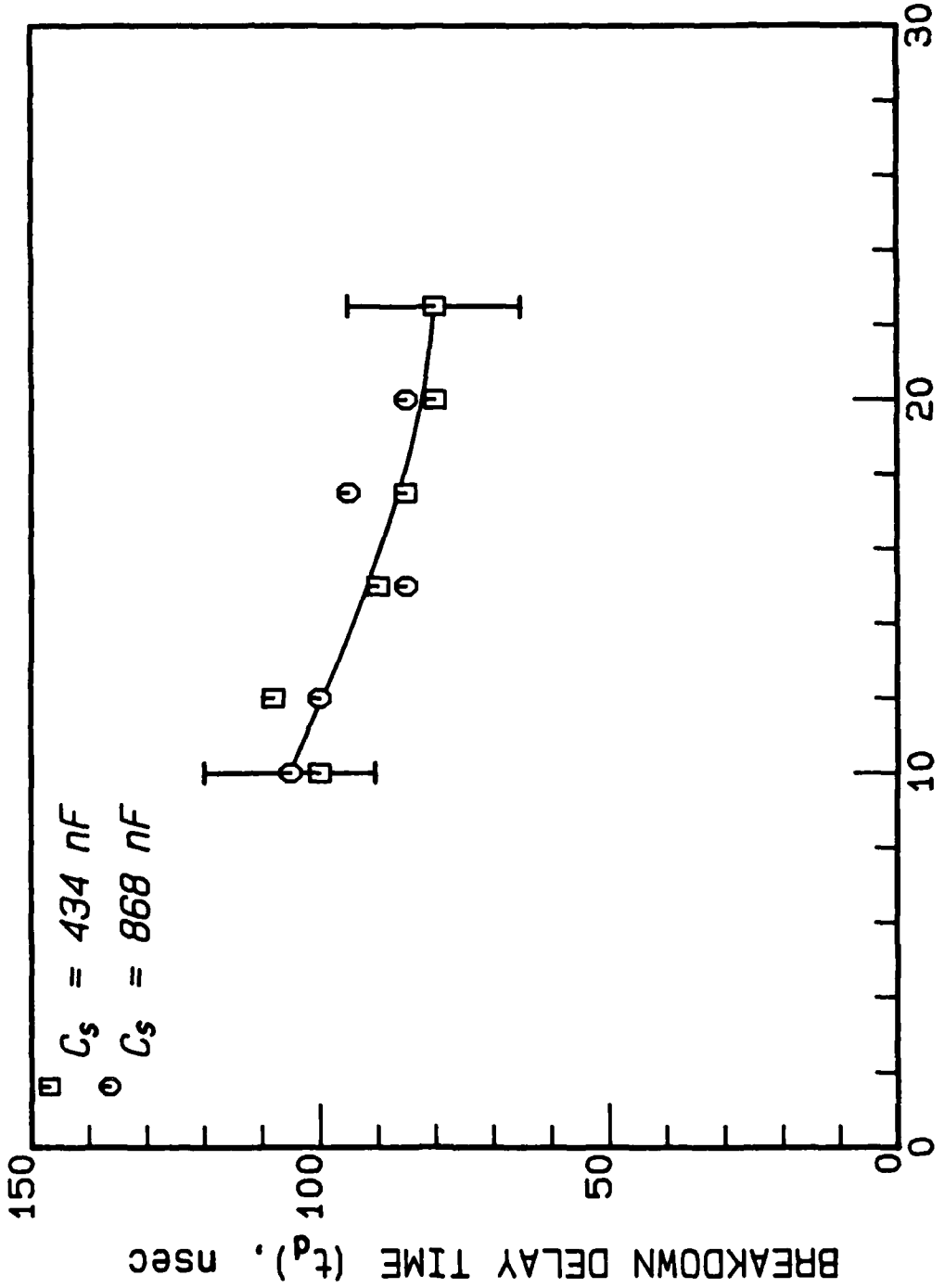

Fig. 11. Delay time (t_d) as a function of charging voltage (V_c).

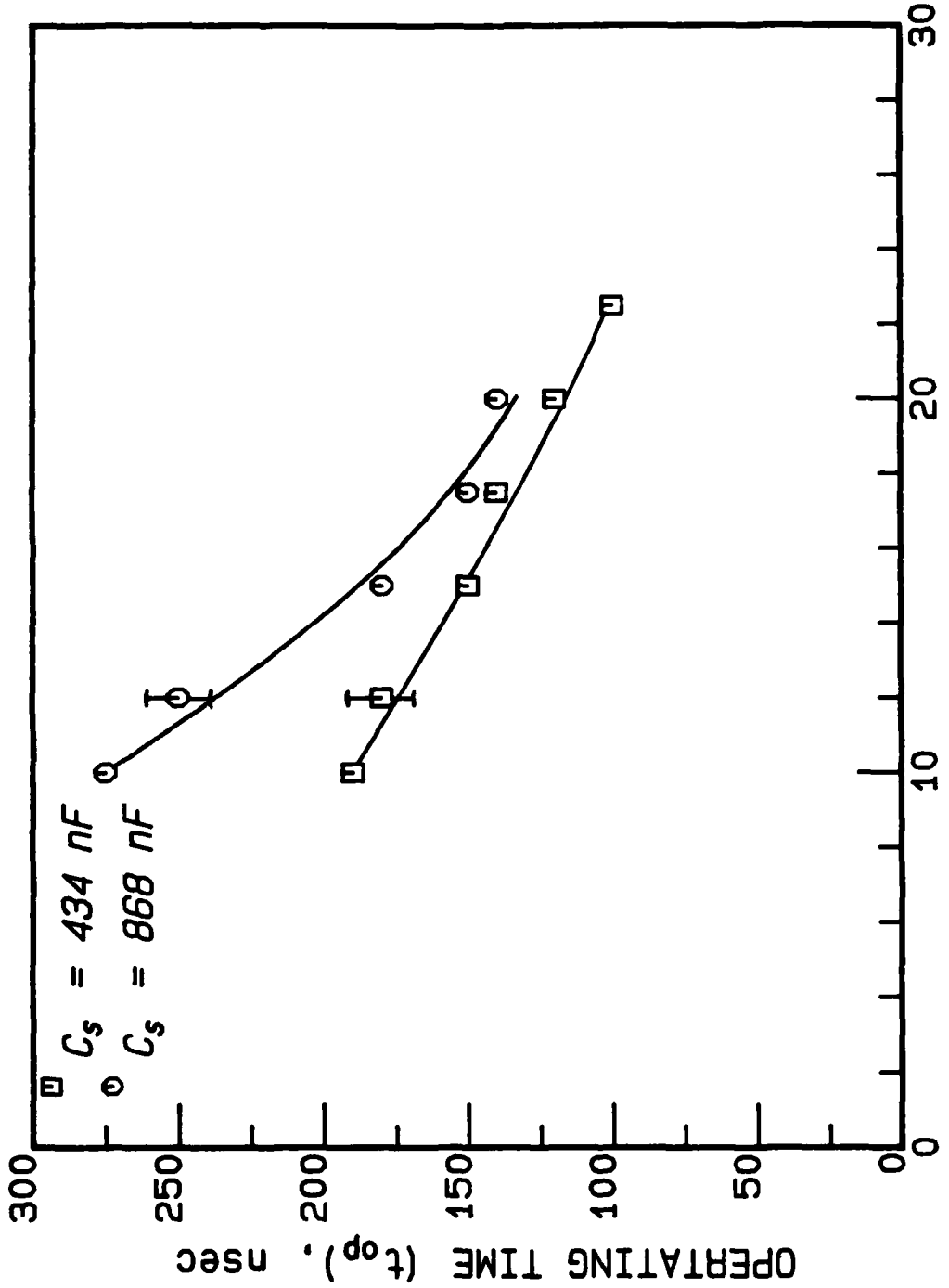

Fig. 12. Operating time (t_{op}) as a function of charging voltage (V_c).

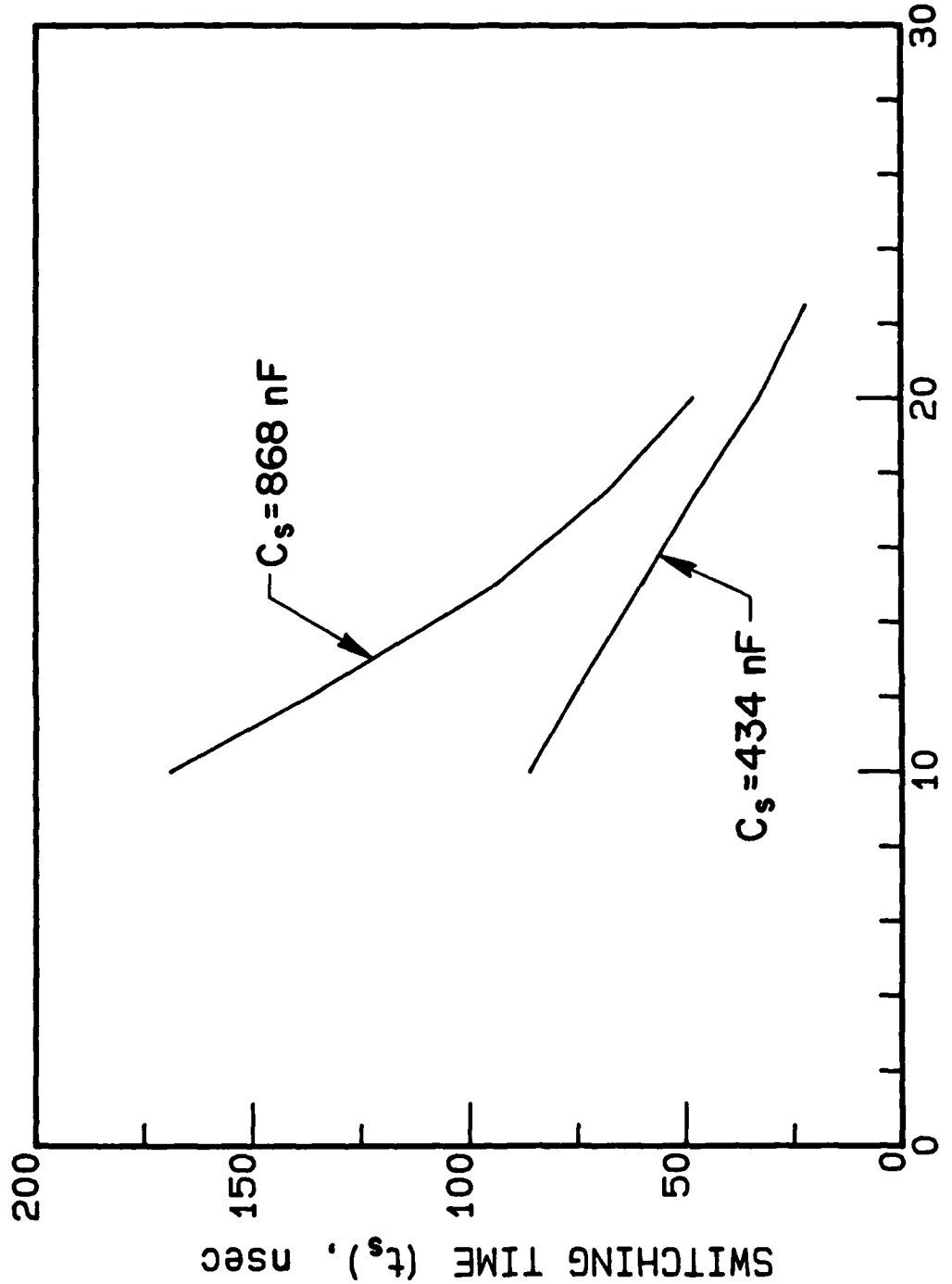

Fig. 13. Switching time (t_s) (inferred) as a function of charging voltage (V_c).

Measurement of Electrical Recovery Characteristics

The recovery of electrical strength in surface-discharge gaps depends in a complicated manner upon the mechanisms of radiation-induced substrate vaporization, plasma recombination kinetics, and conductive channel gasdynamic expansion. The recovery of electrical strength can be measured by injecting a secondary high-voltage pulse of voltage U into the surface-discharge plasma after a preset delay. For various values of U/U_{br}, where U_{br} is the potential required for gap breakdown without a preceding discharge, we define the recovery time t_r as the delay time at which the secondary voltage pulse is reduced in amplitude by 10%, i.e.

$$U(t=t_r) = 0.90\ U(t=0^-), \tag{20}$$

where t=0 is the time at which the main discharge is fired and $U(t=0^-)$ is the voltage amplitude with no preceding main discharge. Note that this definition of t_r is somewhat different from that of Bel'kov and Dashuk [10], where t_r is the delay time at which application of the secondary pulse has a 50% probability of inducing breakdown. The adoption of a modified definition of t_r is necessary because of differences in the experimental method and will be elaborated upon below.

A schematic diagram of the experimental configuration for measurement of recovery time is shown in Fig. 14. As before, C_s and C_p are the main and peaking capacitances, R_c is the charging resistance, L_0 and L_1 are the intrinsic circuit inductances, and S_1 represents two N_2-pressurized spark-gap switches operated in parallel. The secondary pulse is generated after a present delay by a custom-built high-voltage pulser and injected via resistor R_1 (2 kΩ) into the plasma through a tertiary electrode centered between the cathode and anode. The voltage U and current I of the secondary pulse are recorded on a TEK 7704A oscilloscope using voltage probe VP (TEK P6015) and current monitor CM_2 (Ion Physics Company CM-10-M). The hv pulser generates no-load pulses having peak amplitudes up to 36 kV, pulsewidths (FWHM) of 0.8 μsec, and initial rates of voltage rise up to $\sim 6 \times 10^{10}$ V/sec. Use of a well-regulated, precisely adjustable power source (HP 6516A) for the hv pulser insures generation of very accurate, repeatable pulses. Since the hv pulser cannot reliably generate pulses below 4 kV in amplitude, closure of switch S_2 introduces a preset load (R_2 = 1.5 kΩ) into the circuit permitting application of secondary pulses with amplitudes as small as 0.5 kV. Timing of the experiment occurs by the following events: (1) triggering of switch S_1 causes current to flow in the main discharge, (2) current monitor CM_1 (Ion Physics Company CM-1-S), sensing this current, triggers the delay generator (Heath IG-1277) which, in turn, (3) simultaneously triggers both the hv pulser and oscilloscope after a preset delay.

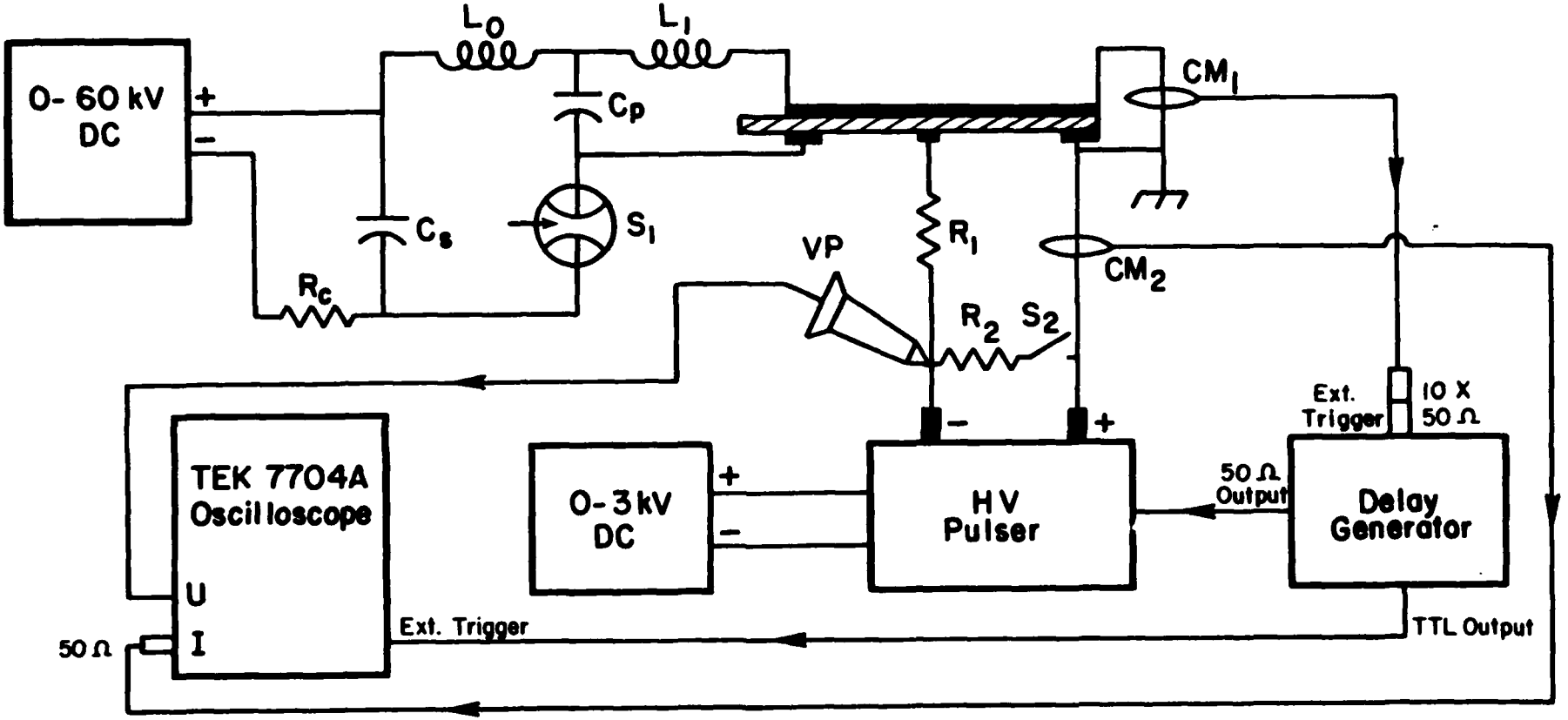

Fig. 14. Schematic diagram of the double-pulse surface-discharge circuit used to determine plasma recovery time.

Surface-discharge source parameters are the same as used previously to measure the characteristic breakdown times, except for the presence of the tertiary electrode. U_{br}, as measured here, is the voltage necessary to just bridge the gap between the tertiary electrode and anode or cathode. For Ar gas at 1 atm pressure and a gap of 4.7 cm, $U_{br} \sim 8$ kV. The results of these measurements are shown by the data in Fig. 15 and 16. The electrical strength of the gap remains low for 100-120 μsec and then recovers very rapidly. These measurements indicate that t_r is insensitive to I_p and C_s over the limited range of values investigated. Direct comparison of these results with those of Bel'kov and Dashuk [10] is not possible because the value of w was not specified and the current density cannot be estimated. Furthermore, the experimental arrangement of Bel'kov and Dashuk permitted application of secondary pulses having a rise time of 2 μsec and duration of 50 μsec by discharge of a second capacitor bank. The discharge plasma was said to have retained its strength if secondary breakdown did not occur within the first 5 μsec of this pulse. Thus, both the method of determination and definition of t_r are substantially different. Qualitatively, however, our measurements agree with the high-current (I_p = 4 kA) data of Bel'kov and Dashuk, who found that the relative strength is low immediately following the main discharge ($< 0.2U_{br}$) and then increases rapidly to values $> 0.6U_{br}$ for the rare gases. The rate of recovery increases with increasing pressure for the rare gases.

Identification of the mechanism which controls plasma recovery is difficult without further study. The characteristic time for gasdynamic motion of the plasma t_{gd} can be estimated from photographic observations of the plasma thickness and measurements of the shock-wave velocity (to be described subsequently). By assuming a rate of expansion of the plasma sheet away from the dielectric substrate which is half the measured shock velocity, a value of $t_{gd} \sim 10$ μsec is obtained. Now the characteristic time for plasma recombination t_{pr} can be estimated using the electron kinetic equation:

$$dn_e/dt = S - (k_a N_a + k_r n_p) n_e \tag{21}$$

where n_e and n_p are the electron and positive-ion densities, S is the electron production source term, N_a is the density of electron attaching species, and k_a and k_r are the rate coefficients for attachment and recombination, respectively. In the recovery phase when the current is zero we assume $S = 0$ and $n_e = n_p$. For an argon plasma, we assume further that the electron kinetics are recombination dominated ($k_a N_a \ll k_r n_p$), so that Eq. (21) may be solved to yield

$$n_e(t) = n_e^o/[k_r n_e^o t + 1]. \tag{22}$$

During the afterglow phase, the electron loss mechanism for the rare gases at high pressure is dominated by dissociative recombination of the dimer ions with electrons:

$$R^+ + R \longrightarrow R_2^+$$

$$R_2^+ + e \longrightarrow R^* + R,$$

and $k_r = 9.1 \times 10^{-7}$ cm^3/sec [11] for Ar at 300 K. The electron density during the high-current discharge phase, n_e^o, was inferred from the Stark broadened linewidth of the H-alpha line at 656.3 nm [12] and found to be 3×10^{16} cm^{-3} for the discharge conditions depicted in Fig. 16. The H-alpha line was present for all discharges across plastic dielectric substrates regardless of the ambient gas atmosphere and provides a useful diagnostic method for determining electron density. If t_{pr} is defined as the time required for the electron density to decrease by 3 orders of magnitude, then a value of 40 nsec is obtained when the numerical values above are inserted into Eq. (22). We note that $t_r \sim 150$ μsec and $t_r >> t_{gd} >> t_{pr}$. Hence, neither electron recombination or plasma expansion seem responsible for recovery of electrical strength in the gap since the characteristic times estimated for both processes are much shorter than the measured value of t_r. One process which has not been considered yet is continued substrate ablation during the afterglow phase and its role in breakdown by closely-spaced, subsequent pulses. Although a model for this process has not been developed, the characteristic time for the temperature of the dielectric surface to drop below the vaporization point after the instantaneous application of an intense uv irradiance is of the order of 100 μsec. Thus, we can speculate that continued substrate ablation, occurring well after the afterglow phase, is responsible for the delay in recovery of electrical strength.

Because the charge stored by the hv pulser in the present experiments is small, breakdown of the gap was not possible in N_2 and air gas environments. Bel'kov and Dashuk [10] found that the rate of recovery is much slower in air than in Ar for identical discharge conditions. The rate of recovery of SF_6:Ar mixtures depends in a complicated way upon the concentration of electronegative gas and total pressure, but the electrical strength immediately following the main discharge is often quite high ($\sim 0.6 U_{br}$).

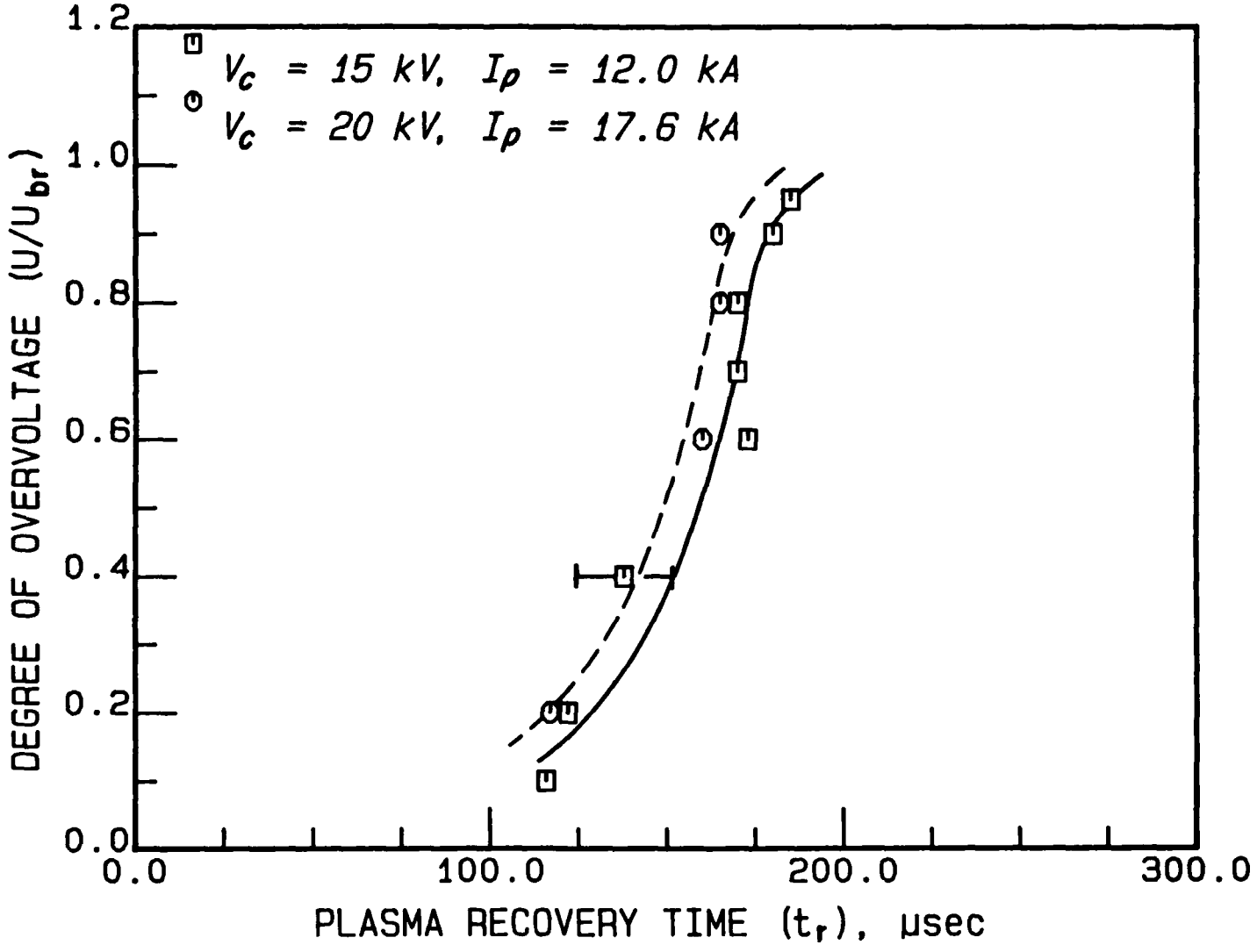

Fig. 15. Recovery of electrical strength after the main current pulse (1 atm Ar, C_s = 434 nF).

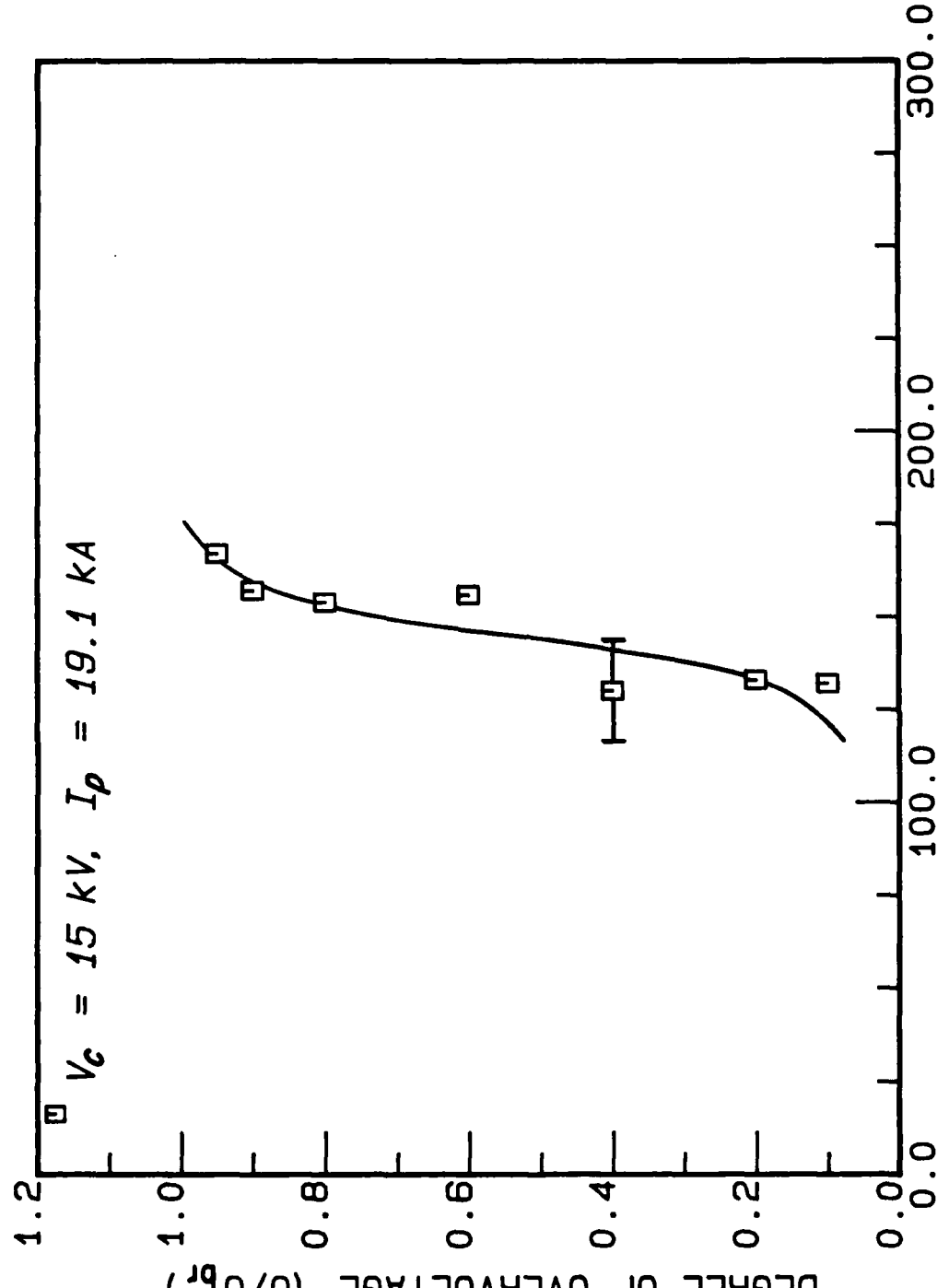

Fig. 16. Recovery of electrical strength after the main current pulse (1 atm Ar, C_s = 868 nF).

SHOCK-WAVE MEASUREMENTS

Shock-Wave Diagnostics

Shock wave velocities were inferred from transit time measurement made using miniature quartz piezoelectric gauges. A typical oscilloscope trace is shown in Fig. 17. The prompt signal is due to electrical noise and serves as a time fiducial while the delayed signal, approximately 80 μsec later, is the pressure pulse signifying arrival of the shock wave. The substrate-to-gauge distance was varied from 3 to 6 cm with no observable decrease in shock velocity.

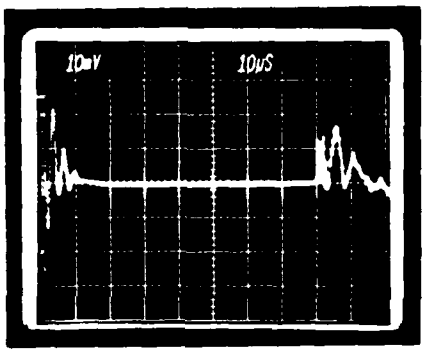

Fig. 17. Typical quartz piezoelectric gauge signal for a 10 x 10 cm^2 planar discharge across cellulose acetate (C_{sp} = 4.2 pF/cm^2) in 1 atm Ar. Electrical parameters are C_s = 868 nF, C_p = 6.6 nF, L = 284 nH and V_c = 14 kV. The gauge is 4 cm from the substrate surface.

Comparison With Shock-Wave Theory

Shock-wave velocities were taken using using discharges with parallel electrodes operating under the following conditions: C_s= 868 nF, C_p= 6.6 nF, L = 284 nH, w = d = 10 cm, and cellulose acetate dielectric (0.76 mm thick). Measured shock velocities D increase slowly with increasing V_c and, hence, with increasing E_s. Comparison with theory requires that we know the discharge power density G (W/cm^2), defined as

$$G = E_d/(At_{eff}), \tag{23}$$

where t_{eff} is the effective pulsewidth of the discharge (which is assumed to be equal to the effective optical pulsewidth, i.e. the width of an equivalent square wave having the same peak power and energy as the actual

pulseshape). E_d is calculated once η_d is known. Data in Figs. 18 and 19 clearly indicate that the plasma resistance is larger with Xe discharges resulting in a higher discharge efficiency η_d, better source-driver impedance matching, and a shorter optical pulsewidth.

The shock velocity produced by a Chapman-Jouguet detonation (such as a laser supported absorption wave) can be described by Raizer's cube-root law [13]:

$$D = [2(\gamma^2 - 1)\, x G/\rho]^{1/3}, \tag{24}$$

where γ is the ratio of specific heats, ρ is the gas density and x is the fraction of discharge power which goes into generation of the shock. Shock velocity data as a function of stored energy are shown in Fig. 20. Instead, if we plot these same data as a function of the discharge power density input to the plasma and assume that 2.7% and 0.6% of that power is allocated to the shock for the Ar and Xe discharges, respectively, then we observe good agreement between Raizer's formula (solid lines) and experiment (data points) as shown in Fig. 21. More importantly, the slopes of the measured shock velocities, determined by least-squares fitting, are equal to 0.32 and 0.31 for Ar and Xe gas, respectively, in good agreement with the theoretical value of 0.33.

The parameter x in Eq. (24) was found by adjustment until agreement with experiment (Fig. 21) was achieved. No readily apparent analytical method exists for determining x <u>a priori</u>. Andreev et al. [14] developed a numerical method for computing the electrical, radiative, and gasdynamic behavior of a surface-discharge initiated inverse z-pinch based on the "electrotechnical" approximation in one-dimension. Although the geometry used here (planar) differs from that of the inverse z-pinch (cylindrical), qualitative comparisons are justified since both configurations operate in rare gases at high pressure under similar discharge conditions. Andreev's model shows that the radiation flux can significantly alter the shock-wave behavior since the characteristic photon mean free path is comparable to or greater than the thickness of the shock front. Because the photons are absorbed over a layer of appreciable thickness, the shock wave is not analogous to an optical detonation where energy is absorbed in a thin layer of hot gas behind the shock front. Their results show a temperature profile which remains almost constant at 2-3 eV from the inner radius of the plasma shell until just before the shock front. For a frame of the numerical simulation corresponding to the time of peak current, the peak radiation flux occurs just behind the shock front and the wave is overcompressed, i.e. the observed compression is larger than that predicted at the Jouguet point on an adiabat for a normal detonation. Roughly half of the radiation flux is absorbed in the wave zone due to the high gas density ($\rho/\rho_0 \sim 3$) and comparatively high gas temperature (~1 eV). The observed "superdetonation"

wave velocity is only slightly higher than the normal detonation velocity, however, because of the small slope of the shock adiabats near the Jouguet point.

The data presented here represent the first experimental measurements of shock-wave velocities for planar surface discharges, so there are no other data sources available for comparison. Shock-wave velocities, inferred from streak photographs, were reported for a surface-discharge initiated z-pinch by Andreev et al. [15] and Belousova et al. [16]. When operated at P > 30-50 Torr (identified by these authors as the "gasdynamic" regime), the gaskinetic pressure is roughly comparable to the magnetic pressure and the surface-discharge plasma shell is highly uniform. This plasma shell remains attached to the inner surface of the dielectric cylinder, although the shock wave detaches from this shell and converges toward the axis with a velocity which can be as much as twice the expansion velocity of the shell. Typical shock velocities measured by these authors for operation at P = 1 atm are D = 1.3×10^5 cm/sec for Xe [15] and D = $1.0(0.6) \times 10^5$ cm/sec for Xe(Ar) [16]. The measured shock velocity was observed to be inversely proportional to the product of z-pinch radius and square root of the initial gas density.

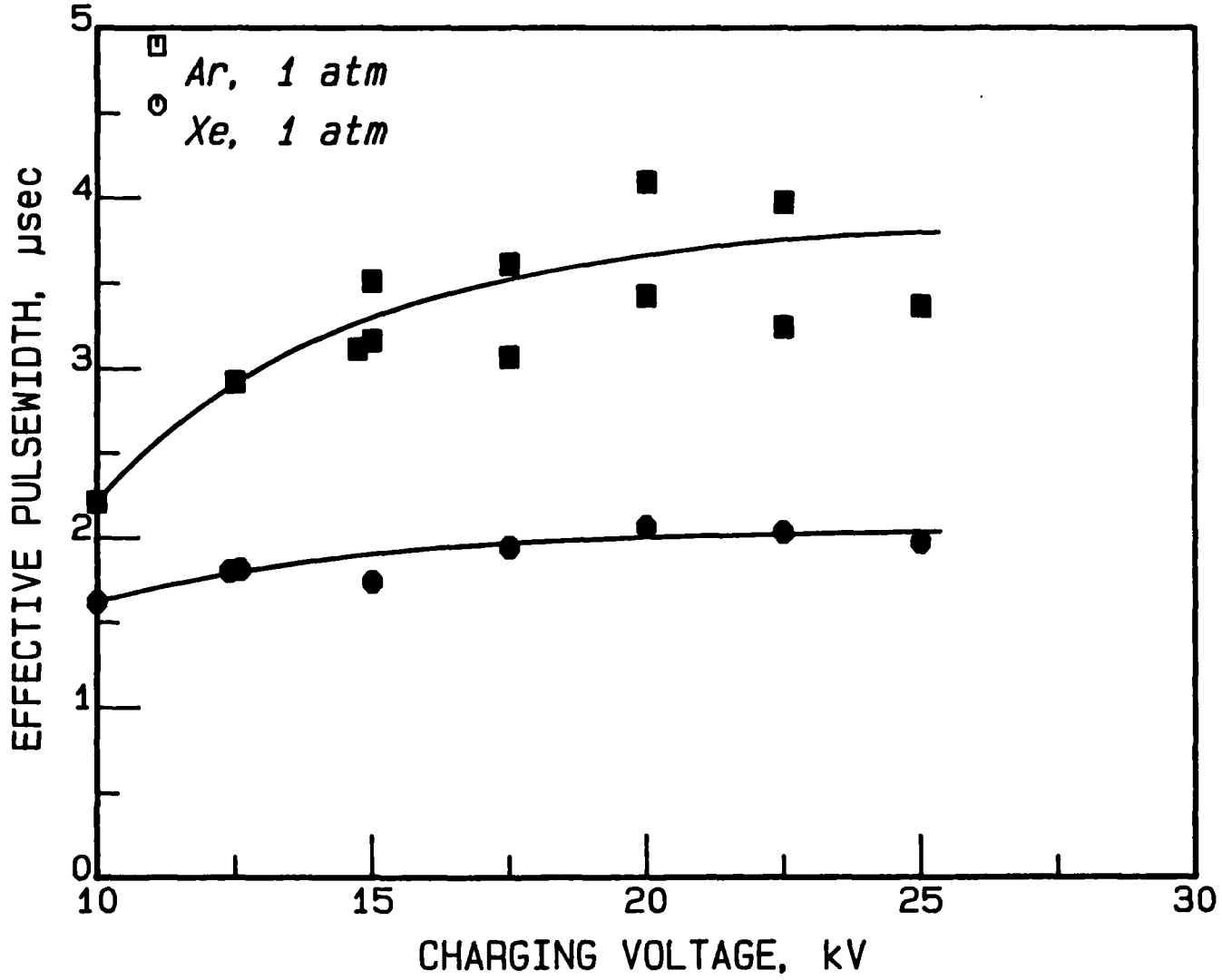

Fig. 18. Effective optical pulsewidth (t_{eff}) as a function of charging voltage (V_c) (w x d = 10 x 10 cm^2).

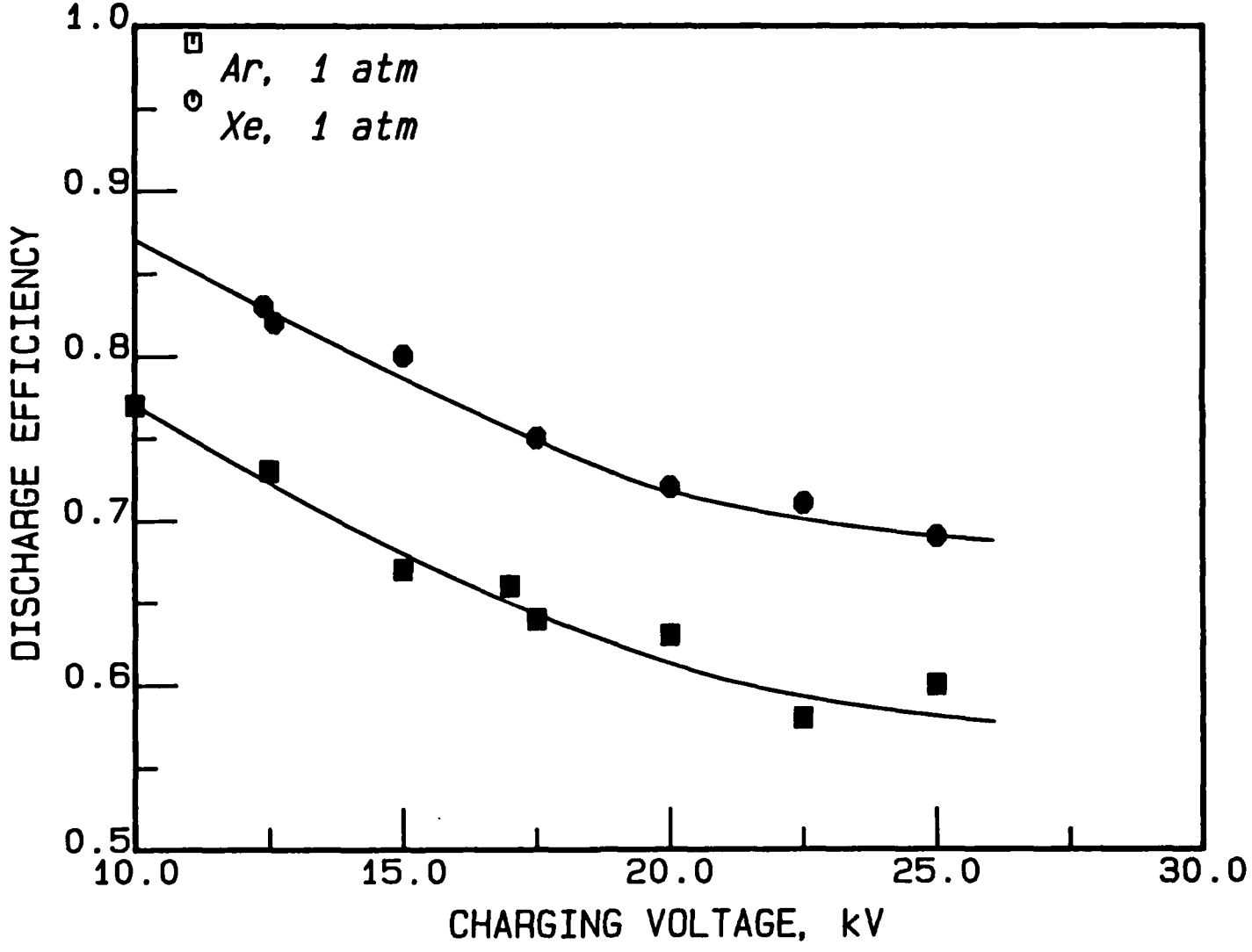

Fig. 19. Discharge efficiency (n_d) as a function of charging voltage (V_c) (w x d = 10 x 10 cm^2).

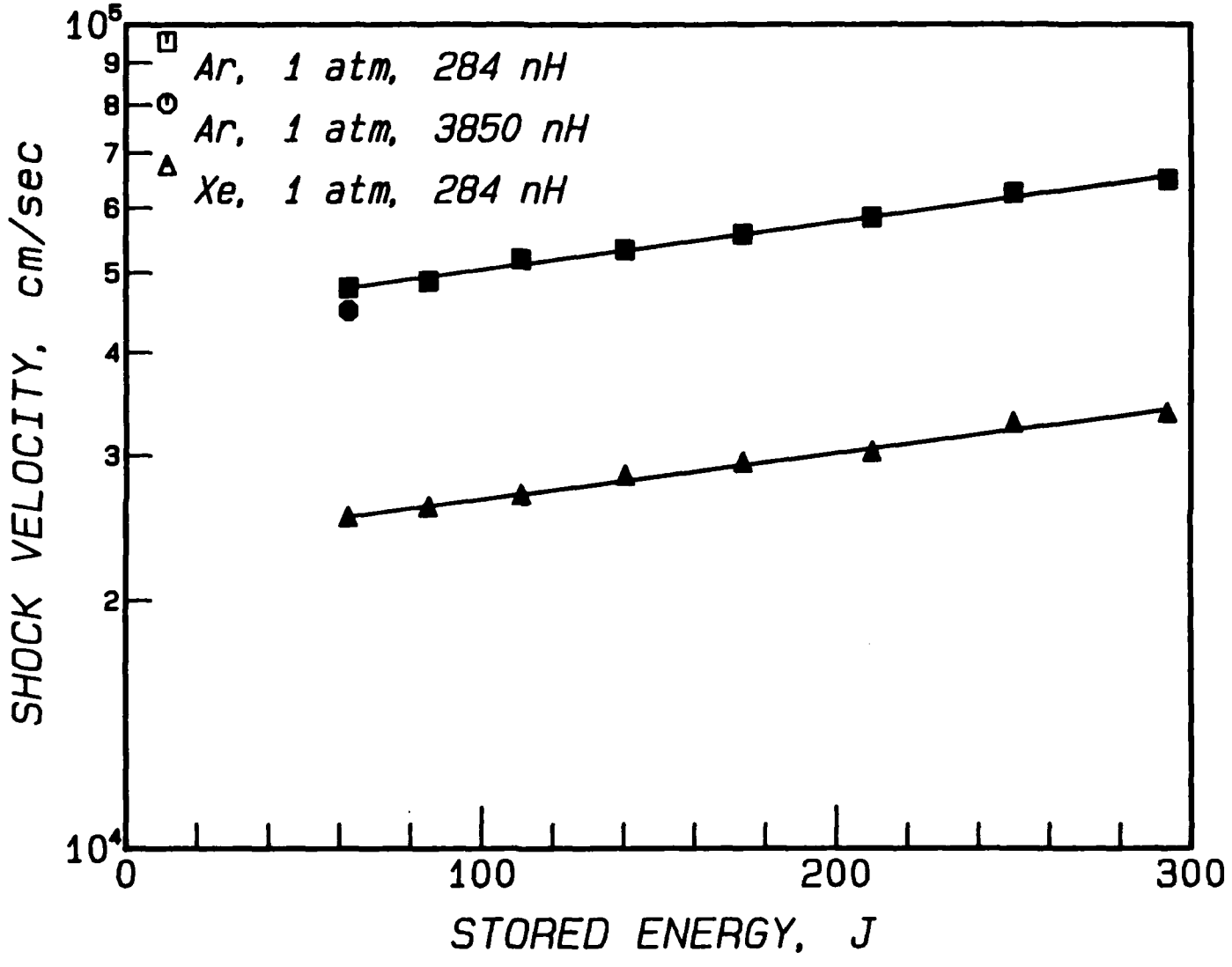

Fig. 20. Shock velocity (D) as a function of stored energy (E_s).

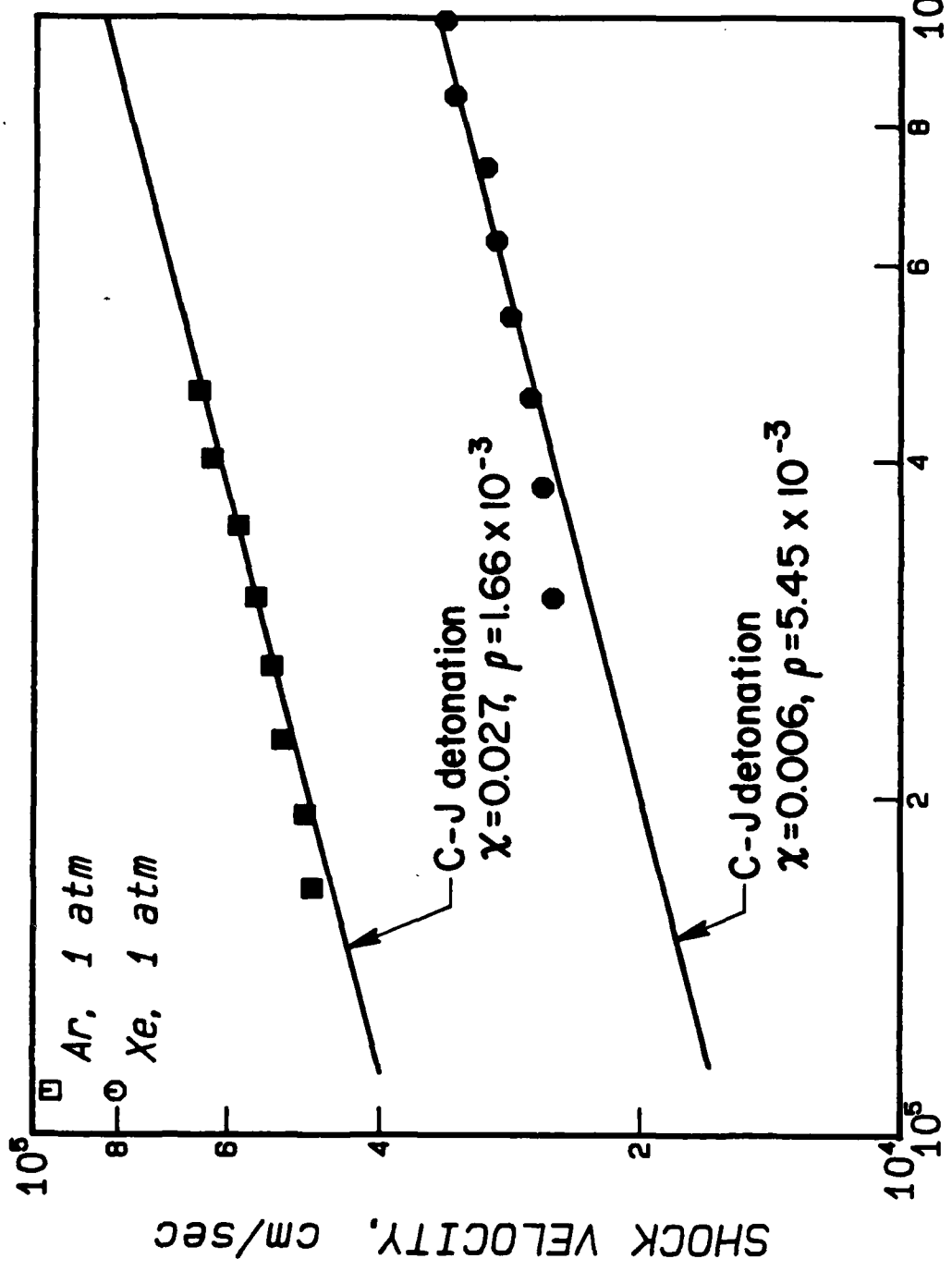

Fig. 21. Shock velocity (D) as a function of discharge power density (G).

NON-BOLTZMANN BEHAVIOR OF EXCITED SPECIES

Non-Boltzmann behavior of excited species in a surface-discharge plasma provides opportunities for enhanced radiative output in selected spectral regions and improved radiative efficiency. Since these processes are believed to be due to recombination cooling effects, lasing may be possible. Such lasers would resemble the segmented-plasma excitation-recombination devices of Silfvast and co-workers [17-19] at Bell Laboratories except that the vaporized and excited species originate from the substrate rather than the electrodes. Numerous strontium lines were observed from surface discharges across a strontium titanate substrate in previous experiments performed by the present author [5], and the possibility of achieving a population inversion on the $6^2S_{1/2} - 5^2P_{3/2}$ or $6^2S_{1/2} - 5^2P_{1/2}$ transitions in Sr II is investigated here.

Recombination lasers based on these transitions have been built and are reasonably well understood [20-24]. An energy level diagram for the Sr II ion is shown in Fig. 22. Impact-radiative recombination of Sr^{2+} populates the upper levels of the Sr^+ ion. The transitions above, however, terminate on resonance levels. Under normal circumstances, the 5^2P resonance levels should be effectively filled by cascades from higher D and S levels and by self-absorption of the $5^2P_{3/2,1/2} - 5^2S_{1/2}$ resonance transitions. The close proximity of the $4^2D_{5/2,3/2}$ levels to the 5^2P levels, however, provides a means by which electron superelastic collisions can act to depopulate the lower laser level. Lasing is therefore possible on the $6^2S_{1/2} - 5^2P_{3/2,1/2}$ transitions producing emission at 430.55 nm and 416.18 nm, respectively, as shown by the dark lines in Fig. 22. General theoretical considerations for pulsed operation of plasma recombination lasers are given by Zhukov et al. in Ref. [21] and specific kinetics of the Sr II lasing system are given by these authors in Ref. [22].

Experiments were performed using strontium titanate and strontium zirconate substrates with an active area $A = w \times d = 4 \times 6$ cm^2 and a thickness = 5 mm (Table II). Parallel electrodes made of stainless steel were used. Each substrate was bonded to a stainless-steel backplane which was mounted within a recess in a Plexiglas® holder. The surface discharge source was located within a stainless-steel chamber and fed using RG-217/U cable as described in Table III. All experiments were conducted with parallel electrodes and electrical parameters $C_s = 868$ nF, $C_p = 0$, $\eta_d \sim 0.2$-0.3 and $C_{sp} \sim 20$-50 pF/cm^2. The experimental arrangement permitted spectroscopic studies to be performed with the slit image located both perpendicular and parallel to the substrate, with the latter measurements conducted at incremental distances from the surface. In this coordinate system (Fig. 1), x is the distance from the cathode, y is the distance from the centerline in the plane of the

discharge, and z is the distance perpendicular to the substrate. Unless otherwise specified, all measurements with the slit image perpendicular to the surface were taken at the center of the discharge (x = 3 cm, y = 0 cm).

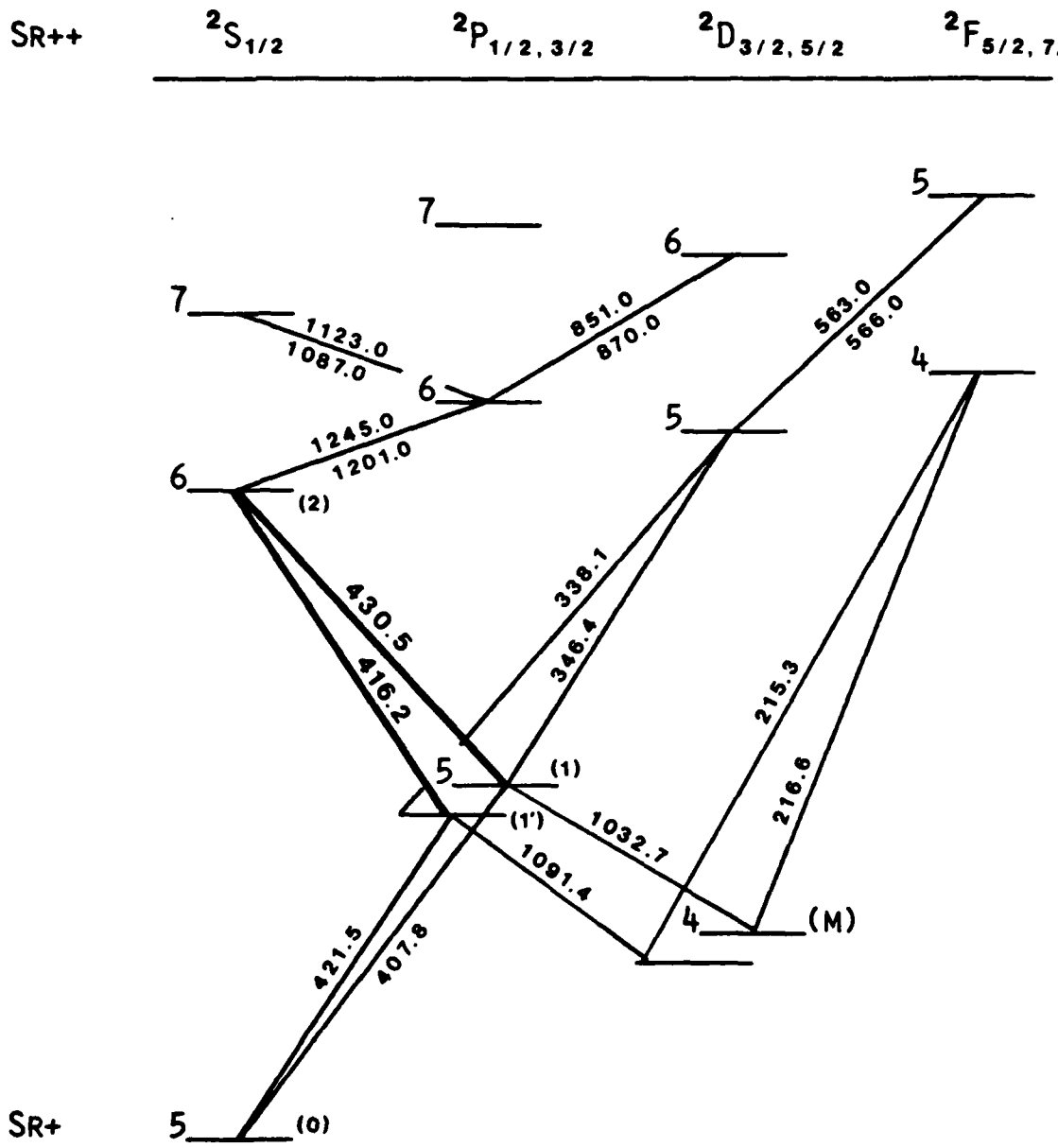

Fig. 22. Energy level diagram of the Sr II ion.

Low-resolution spectra taken with the two substrate materials under identical discharge conditions (Fig. 23) reveal considerable line structure below 520 nm, but unambiguous identification of individual lines is not possible. A comparison of these spectra shows a remarkable similarity in line features with emission from the $SrZrO_3$ substrate being weaker than emission from the

$SrTiO_3$ substrate. This effect can be directly attributed to differences in vaporization temperatures between the two substrates and the corresponding differences in mass ablation rates. High-resolution spectra taken in the region of interest (~400 nm) permitted identification of neutral and singly-ionized lines attributable to the gas atmosphere (e.g. Ar I, Ar II, He I) and originating from the substrate material (e.g. Sr I, Sr II, Ti I, Ti II, Zr I). Continuum and line emission are both much more intense for discharges in Ar than in He gas atmospheres. As shown by the spectra in Fig. 24, Ar I and Ar II lines are numerous and prominent, and often mask identification of weaker line emission from substrate species. Only the Sr II transitions at 407.77 and 421.55 nm were observed; emission from the prospective laser lines at 416.18 and 430.55 nm was extremely weak as expected from discharges in an Ar diluent.

The results were significantly improved for discharges in a He diluent. As shown by the spectra in Fig. 25(b), the prospective laser lines can be positively identified in the spectrum taken with the slit perpendicular to the substrate surface. The $6^2S - 5^2P$ laser lines are not as bright as the $5^2P - 5^2S$ lines, but the small optical thickness in the perpendicular direction allows the radiation to escape. For spectra taken with the slit image parallel to the substrate surface, no region of enhanced emission from the prospective laser lines could be found. Typically, the $5^2P - 5^2S$ lines are quite prominent while the $6^2S - 5^2P$ lines are greatly attenuated as shown by the spectrum in Fig. 25(a). To determine if plasma conditions are more favorable for excitation of the prospective laser lines in the enhanced-field region, comparative spectra were taken with the (perpendicular) slit image located in the center of the discharge and adjacent to the cathode (Fig. 26). Emission from all Sr lines was considerably weaker for discharges across $SrZrO_3$ than across $SrTiO_3$, and only the $5^2P - 5^2S$ lines showed any degree of enhancement.

The $SrTiO_3$ substrate failed after only 30 or 40 discharges which prevented any further experiments (the $SrZrO_3$ substrate, which is mechanically superior, has survived >200 discharges without the slightest hint of failure). Failure advanced by progressive punch-thru to the backplane at x ~ 1 cm and spectra with the slit parallel to the substrate were unknowingly taken as this process was occurring. Since these results were obtained under uncontrolled circumstances, no data are shown, but the spectra are quite curious. The $6^2S - 5^2P$ laser lines are now approximately equal in intensity to the $5^2P - 5^2S$ lines, and the latter lines are strongly reversed. These results suggest that recombination lasing in a surface-discharge plasma is possible by improvement in the discharge conditions and selection of a more optimum substrate material.

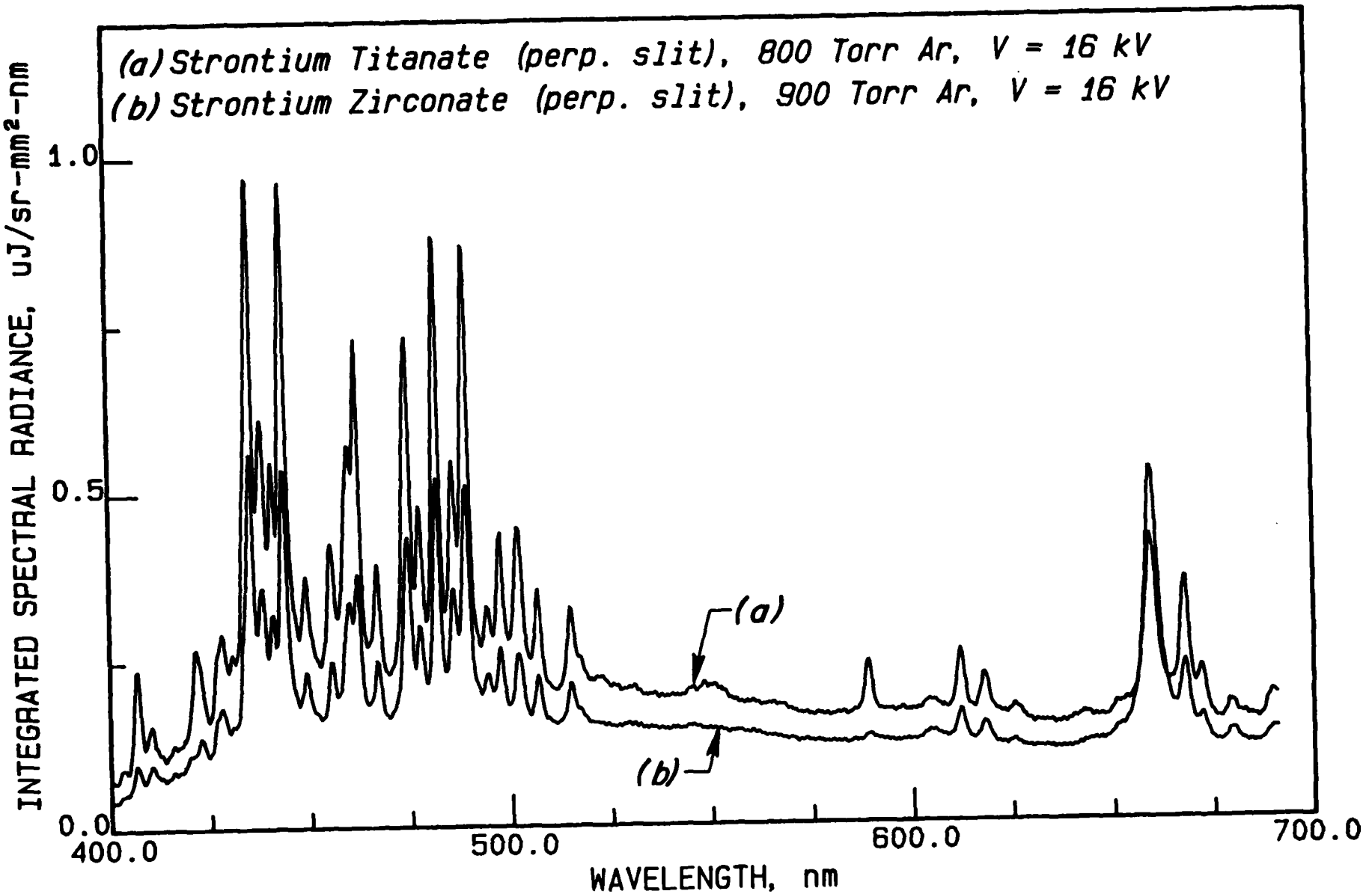

Fig. 23. Low-resolution spectra of surface discharges across strontium-bearing substrates in Ar gas.

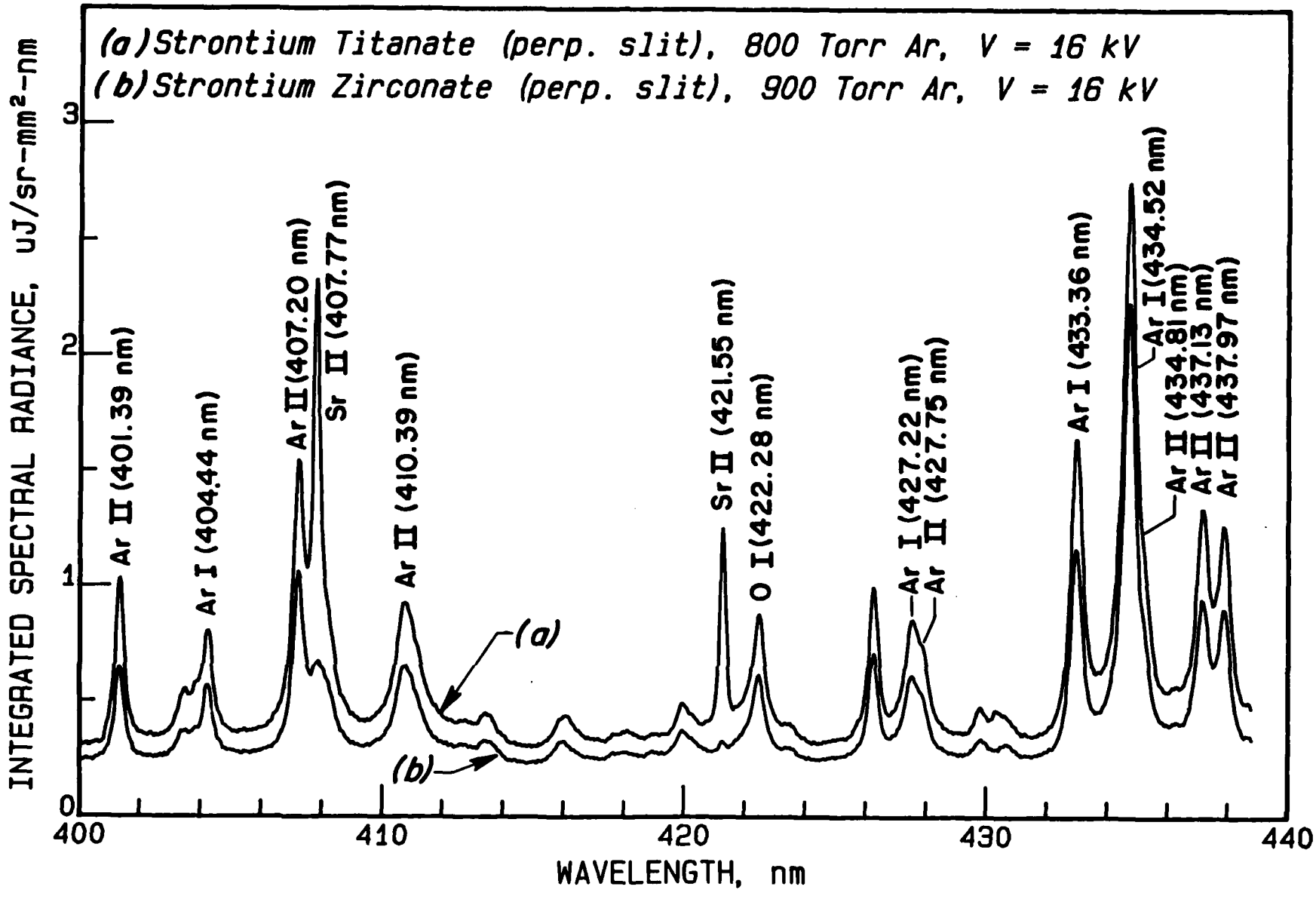

Fig. 24. High-resolution spectra of surface discharges across strontium-bearing substrates in Ar gas.

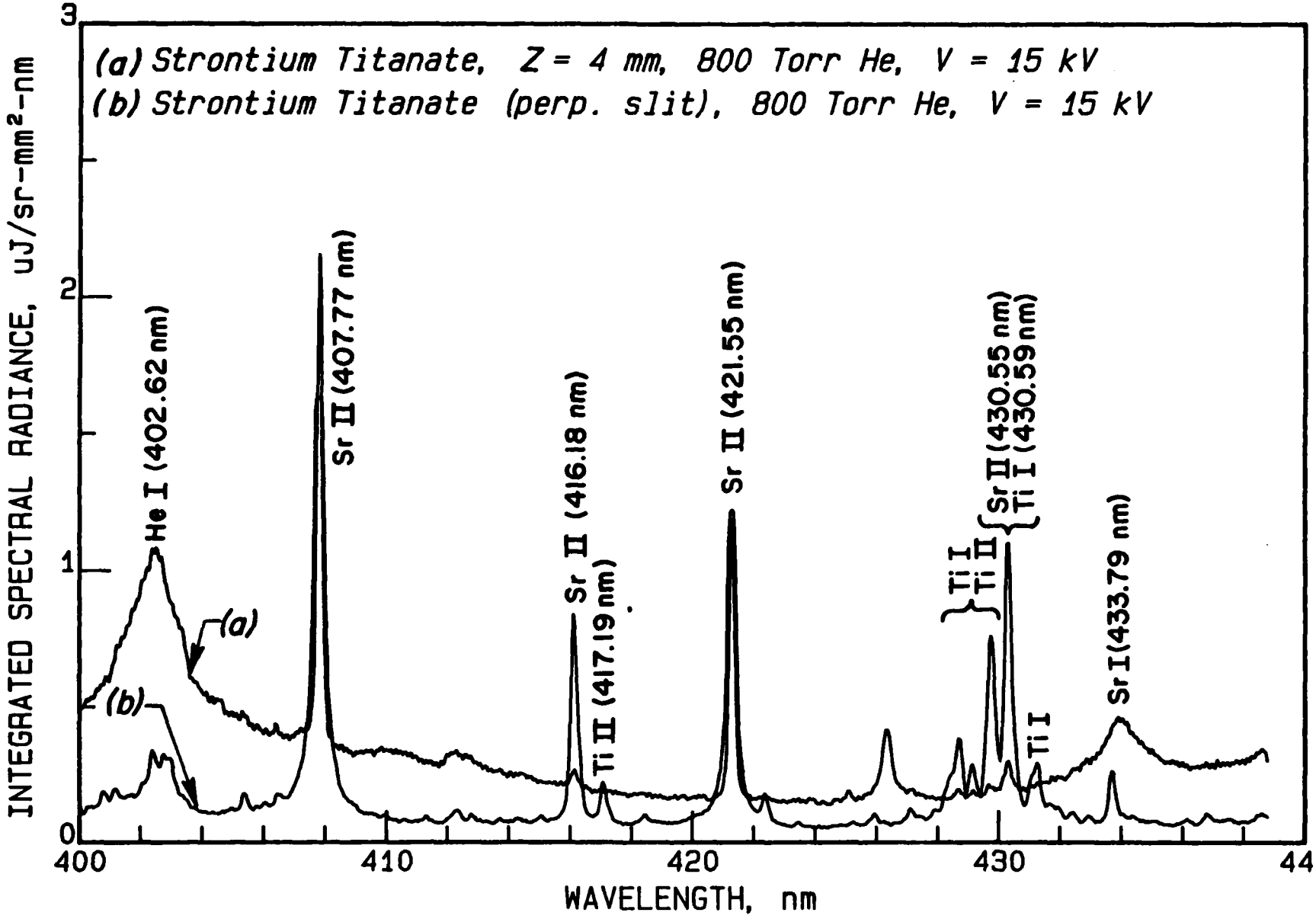

Fig. 25. Comparison of spectra taken perpendicular and parallel to the substrate surface.

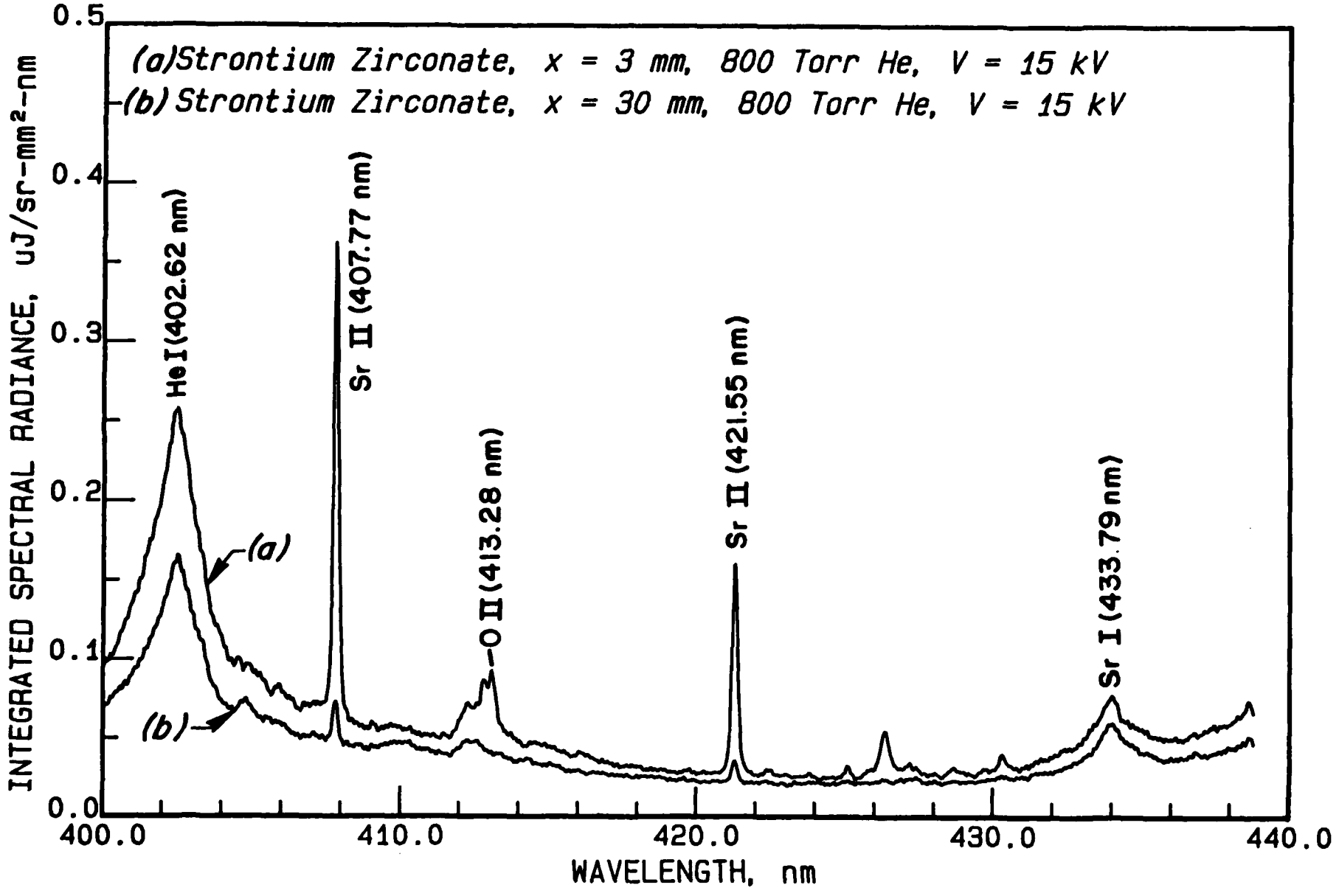

Fig. 26. Comparison of spectra taken adjacent to the cathode and in the center of a surface discharge.

The principal reason for low emission rates on the prospective laser lines is ionization competition between the various plasma species. As shown by the data in Table IV, the ionization potentials for evolved substrate species (Ti, Zr, O) are not significantly larger than for Sr and the population of Sr^{2+} states is expected to be low. A search was conducted to identify other prospective dielectric materials containing strontium bonded with an element or elements with significantly higher ionization potentials. One promising candidate is SrF_2 (density 4.24 g/cm^3, melting point 1473 C, vaporization point 2489 C). From Table IV we see that the first ionization potential for F is over 7 eV larger than the second ionization potential for Sr. Note that operation in a He gas atmosphere with high initial values of T_e increases the concentration of doubly-ionized strontium ions and electrons through the reaction:

$$He^+ + Sr \longrightarrow He + Sr^{2+} + e.$$

TABLE IV. First and second ionization potentials of substrate and gas atmosphere species [25].

Specie	First potential, eV	Second potential, eV
Ar	15.76	27.7
He	24.59	54.38
Sr	5.69	10.38
Ti	6.82	13.6
Zr	6.84	13.1
O	13.61	35.2
F	17.42	35.0

Operation of a surface-discharge plasma recombination laser would also benefit from an increase in n_e during the initial discharge phase [21,22]. This could be accomplished by employing a strip-line electrical transmission line thus reducing L and R_{ext} with a concomitant increase in n_d, $dU/dt|_0$ and I_p. This would have the added benefit of reducing the current pulsewidth. Current and optical pulse waveforms for representative discharges are shown in Figs. 27 and 28. The optical pulsewidths are 4 and 7 μsec (FWHM) for discharges in Ar and He, respectively. Zhukov et al. [21,22] show that it is important for the condition $t_{cd} << t_{tr}$ to be met, where t_{cd} is the current-pulse decay time and t_{tr} is the characteristic recombination time:

$$t_{tr} = 1/(k_{tr} n_e^2). \qquad (25)$$

k_{tr} is the electron-Sr^{2+} recombination coefficient which is proportional to $1/(T_e)^{9/2}$ [22]. From Fig. 28, the 90%-10% optical decay time for a discharge in He diluent is ~30 μsec which is much longer than found in typical longitudinal and transverse discharge-pumped Sr-ion lasers. Also, an increase in n_e during the discharge phase is accompanied by an increase in T_e and it is important that the electron temperature be cooled as quickly as possible during the afterglow [21,22]. No problem exists in increasing the pressure of the He diluent gas in the present surface-discharge arrangement if this should be deemed necessary.

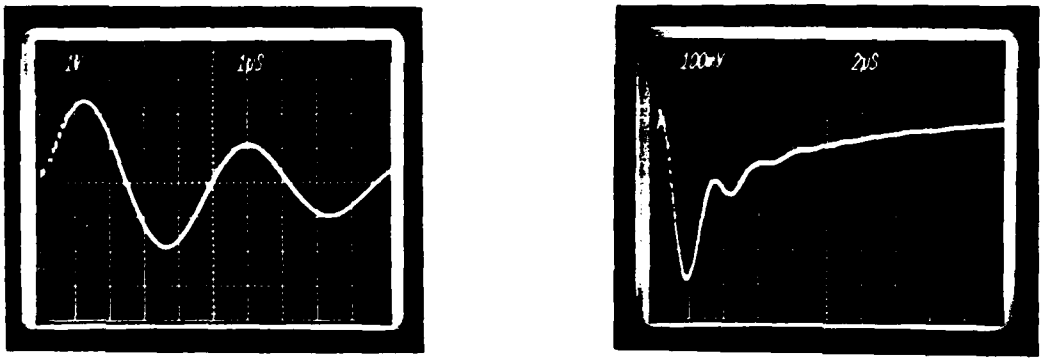

a b

Fig. 27. (a) Current and (b) optical pulse shape (λ = 270 nm, $\Delta\lambda$ = 30 nm) for a 4 x 6 cm^2 discharge across a $SrZrO_3$ substrate (Ar, P = 800 Torr, V_c = 14 kV). The current scale is 1 V = 5 kA.

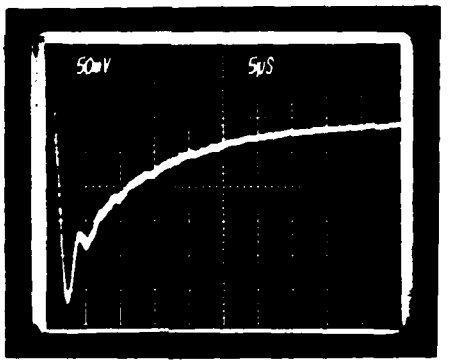

Fig. 28. Optical pulse shape in He gas (P = 800 Torr); other conditions as in Figure 27 except for V_c = 16 kV.

Comparison of data taken with the slit image perpendicular and parallel to the substrate surface permit estimation of the optical thickness which is defined by:

$$\tau(\lambda) = \int k(\lambda)\, dl, \tag{26}$$

where $k(\lambda)$ is the absorption coefficient at wavelength λ and the integral is taken over a finite pathlength in the direction of dl. The thickness of the surface-discharge plasma can be mapped by plotting the integrated spectral radiances for selected line species and continuum emission as functions of slit image height above the substrate surface. Figures 29-31 show plots of these measurements for discharges in Ar and He gas atmospheres (note that these plots are semilogarithmic). It is immediately apparent that discharges in Ar gas are tightly pressed against the substrate (thickness $l \sim 2$ mm), while discharges in He gas are more diffuse and thicker ($l \sim 6$-8 mm). The plasma also becomes more diffuse and extends further away from the substrate as the gas pressure is decreased. For the Ar I line (434.52 nm) under conditions depicted by the spectrum in Fig. 24(b), for example, an optical thickness $\tau = 0.22$ was inferred for emission perpendicular to the substrate surface.

The results shown in Figs. 29-31 indicate that radiation from excited gas-atmosphere and substrate species persists much farther from the surface than does the continuum radiation. For the discharge in Ar gas shown in Fig. 29, Sr II emission is an order of magnitude more intense than the continuum emission for 4 mm < z < 10 mm. Emission from Ar I and Ar II lines is typically a factor of 2 more intense than the continuum for z > 2 mm. For discharges in He atmospheres (Figs. 30 and 31), continuum emission is very weak while emission from He I and Sr I lines decreases slowly as z increases. Radiation from singly-ionized species (e.g. Sr II) falls off more rapidly with z than radiation from neutral species. The high concentrations of neutral and singly-ionized species at large distances from the surface can be attributed to a combination of large radiative lifetimes and additional pumping of higher-energy levels via absorption of uv radiation from the hot, underlying plasma.

Determination of T_e for a plasma in LTE using the ratio of line intensities is a well-known spectroscopic technique. If a number of lines are available for the same ionic species, Boltzmann's graphical method can be used to measure T_e with greater precision since this method is less sensitive to errors in transition probabilities. Furthermore, departure from LTE can be readily identified. T_e is determined from the slope of a best-fit straight line through the points obtained from graphing the relation [26]:

$$\log (I\lambda/A_{ul}g_u) = -E_u/kT_e + \text{constant}, \qquad (27)$$

where I is the line intensity, λ is the transition wavelength (nm), A is the transition probability (Einstein coefficient) (sec^{-1}), E is the energy of the subscripted level (cm^{-1}), k is Boltzmann's constant, and the subscripts u and l denote upper and lower states, respectively. This procedure was employed with the Ar II lines observed in the spectrum shown in Fig. 24(a). Transition probabilities and energy levels were taken from Ref. [27]. Results are shown in Fig. 32, where a best-fit value of T_e = 20,700 K is obtained.

The brightness temperature, T_b, can be estimated by dividing the integrated spectral radiance by the optical pulsewidth and comparing the result with the spectral radiance produced by an ideal blackbody. For discharges across $SrZrO_3$ in Ar gas at atmospheric pressure (V_c = 16 kV), T_b(perpendicular) = 12,300 K and T_b(parallel) = 18,000 K for radiation from the Ar I line at 434.52 nm {see Fig. 24(b) and Fig. 29}. Brightness temperatures for equivalent discharges in He gas are much lower. These data clearly establish that the plasma in planar surface discharges is not opaque even in the soft-uv spectral regions and the observed spectra depart significantly from that of an ideal blackbody. Note that much larger visible-to-near-uv brightness temperatures can be obtained with planar surface discharges by increasing E_d/A [5].

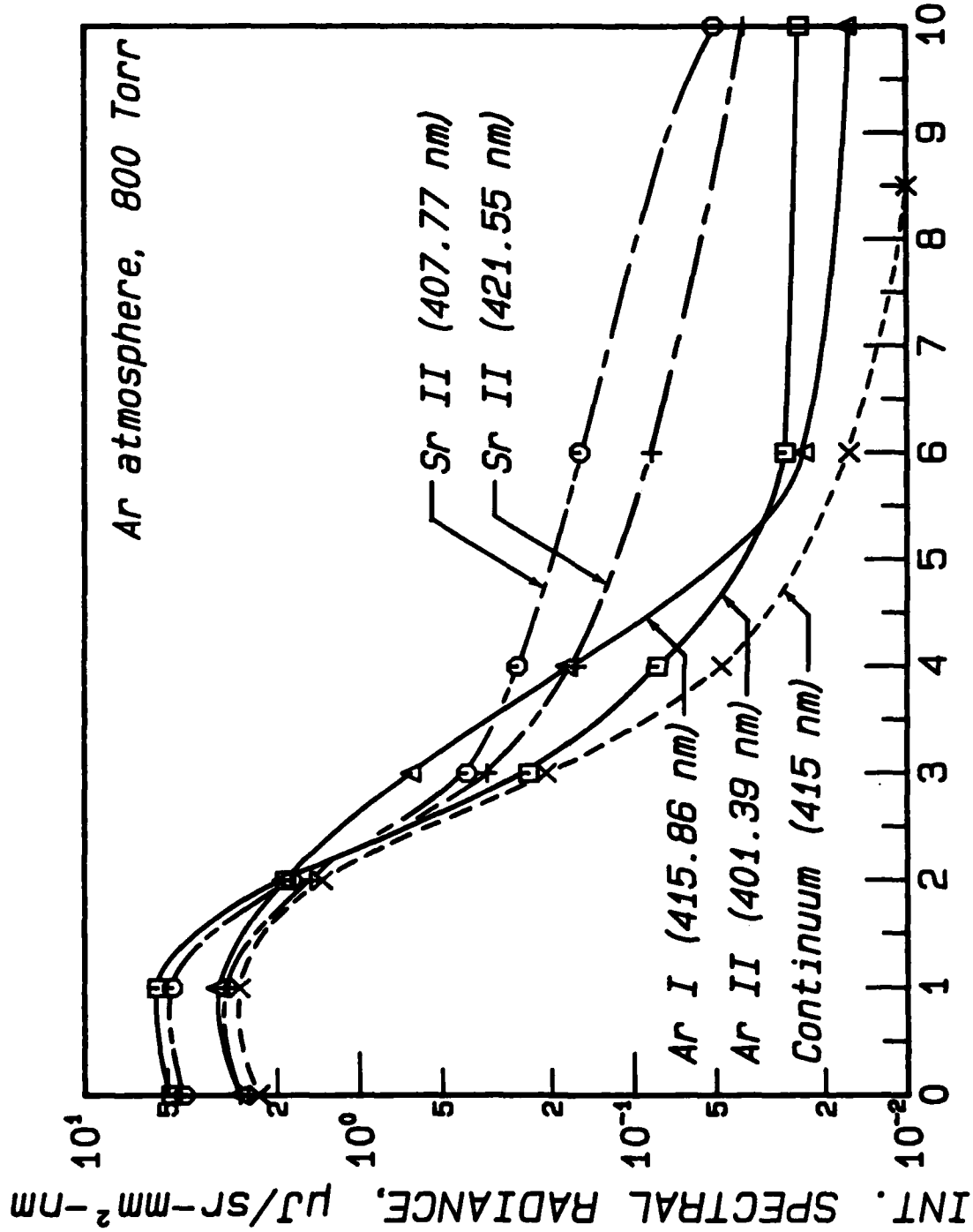

Fig 29. Time integrated spectral radiance for selected emission species observed with a parallel slit orientation ($SrZrO_3$ substrate, Ar gas at 800 Torr, V_c = 16 kV).

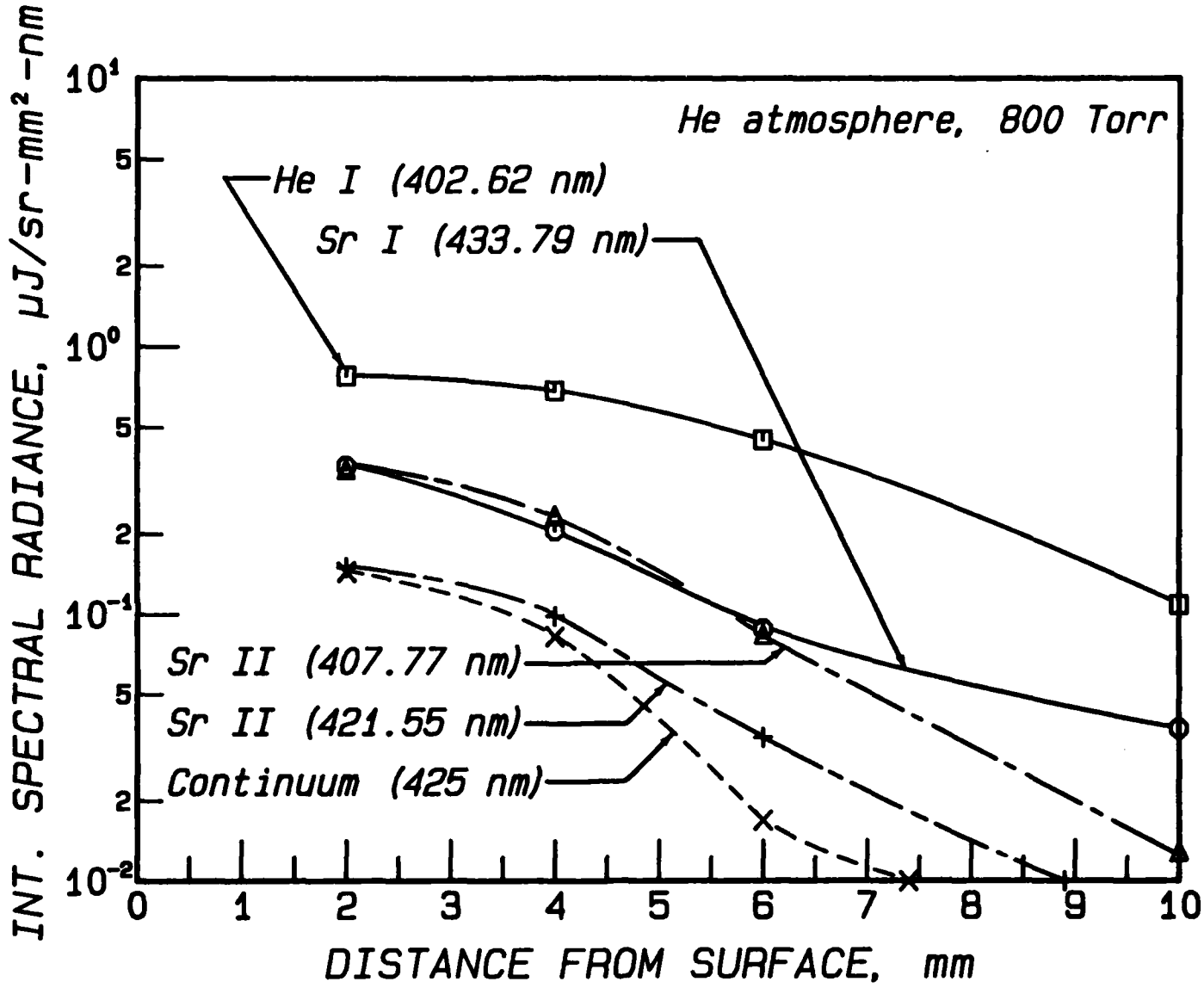

Fig. 30. Time integrated spectral radiance for selected emission species observed with a parallel slit orientation ($SrZrO_3$ substrate, He gas at 800 Torr, V_c = 16 kV).

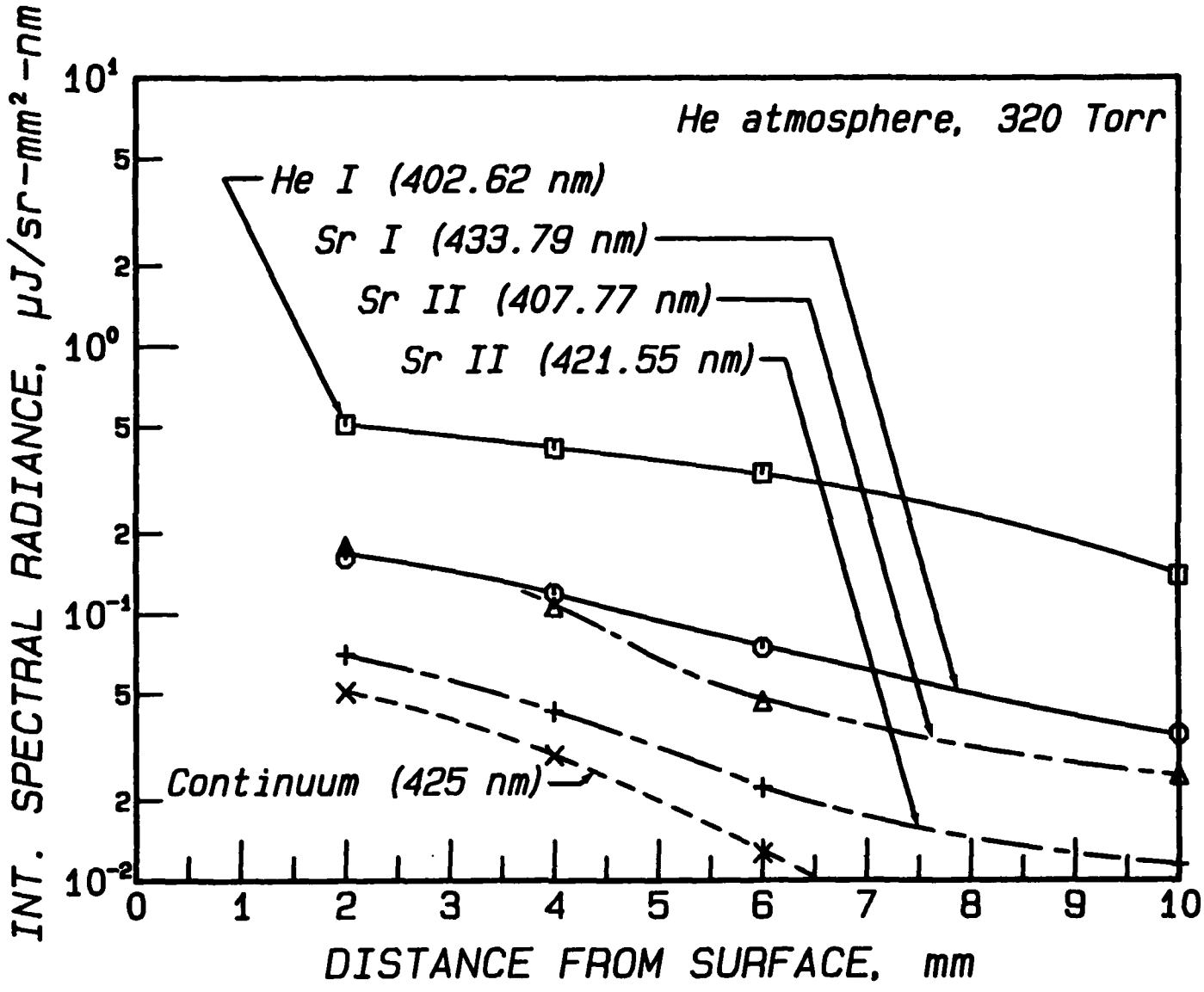

Fig. 31. Time integrated spectral radiance for selected emission species observed with a parallel slit orientation ($SrZrO_3$ substrate, He gas at 320 Torr, V_c = 16 kV).

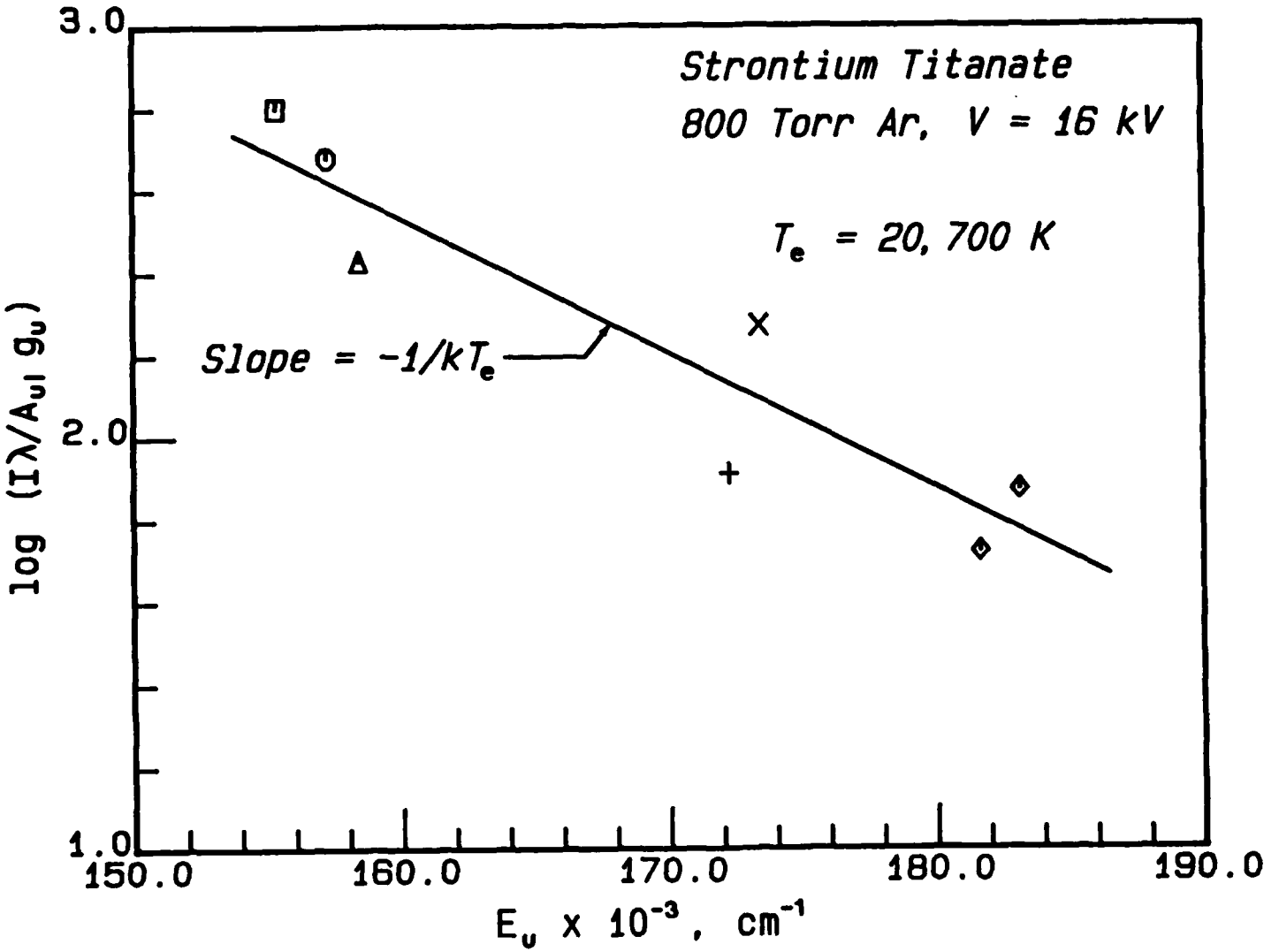

Fig. 32. Boltzmann diagram for Ar II lines observed in the spectrum shown in Figure 24(a).

RECOMMENDATIONS

One certain advantage of surface discharges over other high-intensity optical sources (e.g. exploding wires and foils) is their capability for repetitively-pulsed operation under high energy loadings without catastrophic failure. The present experiments demonstrate that pulse repetition frequencies of at least 1 kHz should be possible for a properly engineered source and specific energy inputs of ~1 J/cm^2 per pulse. The life expectancy of a surface-discharge source is principally limited by erosion of the dielectric substrate. A paucity of erosion-rate data exist in the literature, however, and experimental conditions were not carefully measured where data exist. A research and development effort is needed to identify potential substrate materials which would afford a long life expectancy in optical-source and switch configurations, to construct repetitively-pulsed sources with active cooling through the backplane, and to measure the erosion rate under well-defined discharge conditions. Preliminary estimates based on single-channel erosion measurements made by the present author [3] suggest that life expectancies in excess of 10^6 flashes should be possible for a properly-engineered source operating at E_d/A ~ 1-5 J/cm^2.

Further research is needed to understand the role that radiation transport has on development and propagation of the out-going shock wave. Our results show that the dependence of shock-wave velocity on initial gas density and input power density is adequately described by a Chapmann-Jouguet detonation. This occurrence may be fortuitous, however, since the shock physics here may depart substantially from that of an optical detonation. The state-of-the art in numerical modeling of coupled plasma gasdynamics, radiation transport, and surface ablation is sufficiently advanced that development of a comprehensive simulation is possible. The development of such a model would greatly benefit optimization of advanced optical sources based on surface discharges.

We remain optimistic that a plasma recombination laser based upon a surface discharge can be developed. The discharge conditions during this exploratory investigation were far from ideal. These experiments should be repeated using a different substrate (e.g. SrF_2) to enhanced the population of Sr^{2+} ions. Electrical parameters should be redesigned to produce a higher-power, shorter duration discharge. This could be accomplished by installing a strip-line feed in the present experimental arrangement to decrease total circuit inductance and external loss resistance and by operating at a higher charging voltage. Increasing the He diluent pressure to 2-3 atm should increase the rate of electron temperature cooling.

PUBLICATIONS

Publications of work funded in part by this program are as follows:

R. E. Beverly III, "Incoherent optical pump sources for lasers based on surface discharges," First Int. Laser Sci. Conf. (Dallas, Texas, 18-22 Nov. 1985).

R. E. Beverly III, "Shock waves induced by planar surface discharges," Proc. XVII Int. Conf. on Phenomena in Ionized Gases (Budapest, Hungary, 8-12 July 1985), pp. 562-564.

R. E. Beverly III, "Large-area short-pulse surface discharges for laser excitation," Proc. Int. Conf. LASERS 84 (San Francisco, 26-30 Nov. 1984), pp. 732-739.

ACKNOWLEDGEMENTS

Machining and fabrication of much of the apparatus used in these experiments was expertly performed by B. E. Heller and J. K. Anthony. The contributions of N. E. Cameron, E. S. Molnar, and P. E. Hamilton to preparation of this report are gratefully acknowledged. Thanks go to Dr. R. W. Conrad and J. J. Ehrlich of the U. S. Army Missile Command for loan of the Tracor-Northern DARSS system. Assistance given by M. Colton of Cerac, Inc. in fabrication of the ceramic substrates is also appreciated.

REFERENCES

1. R. E. Beverly III, in Progress in Optics, Vol. XVI, ed. E. Wolf (North-Holland, Amsterdam, 1978), pp. 355-411.

2. R. E. Beverly III, Proc. Int. Conf. LASERS 84 (San Francisco, California, 26-30 November, 1984), pp. 732-739.

3. R. E. Beverly III, Inst. Phys. Conf. Ser. No. 72, 271-276 (1984).

4. T. Y. Chang, Rev. Sci. Instrum. 44, 405 (1973).

5. R. E. Beverly III, R. B. Schaefer, D. G. Youmans, and T. W. Hilton, Final Technical Report to Directed Energy Directorate, U. S. Army Missile Command, Contract Number DAAH01-83-D-A017 (Work Orders 3 and 4), November, 1983.

6. R. E. Beverly III, Final Technical Report to Directed Energy Directorate, U. S. Army Missile Command, Contract Number DAAH01-84-D-A007 (Work Order 4), May, 1985.

7. G. I. Belyaev, P. N. Dashuk, and M. A. Chernov, Sov. Phys. Tech. Phys. 24, 578 (1979).

8. S. I. Andreev, E. A. Zobov, A. N. Sidorov, and V. D. Kostovsov, J. Appl. Mech. Tech. Phys. 21, 103 (1980).

9. D. L. Johnson, J. P. Vandevender, and T. H. Martin, IEEE Trans. Plasma Sci. PS-6, 204 (1980).

10. E. P. Bel'kov and P. N. Dashuk, Sov. Phys. Tech. Phys. 25, 1354 (1980).

11. Y.-J. Shin and M. A. Biondi, Phys. Rev. A 17, 868 (1978).

12. H. R. Griem, Plasma Spectroscopy (McGraw-Hill, New York, 1964), Ch. 14-2.

13. Yu. P. Raizer, Sov. Phys. JETP 21, 1009 (1965).

14. S. I. Andreev, V. Ya. Gol'din, E. A. Zobov, N. N. Kalitkin, V. G. Sokolov, and B. N. Chetverushkin, Sov. Tech. Phys. Lett. 2, 234 (1976).

15. S. I. Andreev, O. G. Baikov, P. N. Dashuk, and P. G. Popov, Sov. Phys. Tech. Phys. 22, 691 (1977).

16. I. M. Belousova, O. B. Danilov, P. N. Dashuk, S. A. Tul'skii, L. L. Chelnokov, and I. L. Yachnev, Sov. Phys. Tech. Phys. 24, 907 (1979).

17. W. T. Silfvast, L. H. Szeto, and O. R. Wood II, Appl. Phys. Lett. 36, 615 (1980).

18. W. T. Silfvast and O. R. Wood II, Opt. Lett. 7, 34 (1982).

19. J. J. Macklin, O. R. Wood II, and W. T. Silfvast, IEEE J. Quantum Electron. QE-18, 1832 (1982).

20. E. L. Latush and M. F. Sem, Sov. Phys. JETP 37, 1017 (1973).

21. V. V. Zhukov, E. L. Latush, V. S. Mikhalevskii, and M. F. Sem, Sov. J. Quantum Electron. 7, 704 (1977).

22. V. V. Zhukov, V. S. Kucherov, E. L. Latush, and M. F. Sem, Sov. J. Quantum Electron. 7, 708 (1977).

23. M. Brandt, Appl. Phys. Lett. 42, 127 (1983).

24. M. S. Butler and J. A. Piper, Appl. Phys. Lett. 42, 1008 (1983).

25. B. M. Smirnov, Physics of Weakly Ionized Gases (Mir, Moscow, 1981), Appendix A6.

26. F. Cabannes and J. Chapelle, in Reactions Under Plasma Conditions, Vol. I, ed. M. Venugopalan (Wiley-Interscience, New York, 1971), pp. 367-469.

27. W. L. Wiese, M. W. Smith, and B. M. Glennon, Atomic Transition Probabilities, Vol. II, NSRDS-NBS 22 (U.S. Government Printing Office, Washington, DC, 1969).

END

FILMED

3 -86

DTIC